TECHNISCHE UNIVERSITÄT
KAISERSLAUTERN

SCHRIFTEN ZUR

FUNKTIONALANALYSIS UND GEOMATHEMATIK

W. Freeden, T. Fehlinger, M. Klug,
D. Mathar, K. Wolf

Classical Globally Reflected Gravity Field Determination in Modern Locally Oriented Multiscale Framework

Bericht 39 – September 2008

FACHBEREICH MATHEMATIK

Classical Globally Reflected Gravity Field Determination in Modern Locally Oriented Multiscale Framework

W. Freeden[1]*, T. Fehlinger[1], M. Klug[1], D. Mathar[1], and K. Wolf[1]

[1] University of Kaiserslautern
Geomathematics Group
67663 Kaiserslautern
P.O. Box 3049
Germany

Dedicated to Kurt Lambeck, President of the Australian Academy of Science

The purpose of this paper is the canonical connection of classical global gravity field determination following the concept of Stokes (1849), Bruns (1878), and Neumann (1887) on the one hand and modern locally oriented multiscale computation by use of adaptive locally supported wavelets on the other hand. Essential tools are regularization methods of the Green, Neumann, and Stokes integral representations. The multiscale approximation is guaranteed simply as linear difference scheme by use of Green, Neumann, and Stokes wavelets, respectively. As an application, gravity anomalies caused by plumes are investigated for the Hawaiian and Iceland areas.

1 Introduction

Gravity as observed on the Earth's surface is the combined effect of the gravitational mass attraction and the centrifugal force due to the Earth's rotation. The force of gravity provides a directional structure to the space above the Earth's surface. It is tangential to the vertical plumb lines and perpendicular to all level surfaces. Any water surface at rest is part of a level surface. As if the Earth were a homogeneous, spherical body gravity turns out to be constant all over the Earth's surface, the well-known quantity $9.81\ \mathrm{ms}^{-2}$. The plumb lines are directed towards the Earth's center of mass, and this implies that all level surfaces are nearly spherical, too. The gravity decreases from the poles to the equator by about $0.05\ \mathrm{ms}^{-2}$. This is caused by the flattening of the Earth's figure and the negative effect of the centrifugal force, which is maximal at the equator. The level surfaces ideal reference surfaces, for example, for heights.

The traditional concept of physical geodesy (cf., e.g., [36]) is based on the assumption that all over the Earth the position (e.g., latitude and longitude) and scalar gravity g are available. Moreover, it is common practice that the gravitational effects of the sun and moon and of the Earth's atmosphere are accounted for by means of corrections. The gravitational part of the gravity potential can then be regarded as a harmonic function. A classical approach to gravity field modeling was conceived by G.G. Stokes (1849). He proposed reducing the given gravity accelerations from the Earth's surface to the geoid. As the geoid is a level surface, its potential value is constant. The difference between the reduced gravity on the geoid and the reference gravity on the so-called normal ellipsoid is called the gravity anomaly. The disturbing potential, i.e., the difference between the actual and the reference potential, can be obtained from a (third) boundary value problem of potential theory. Its solution is representable in integral form, i.e., by the Stokes integral. The disadvantage of the Stokes approach is that the reduction to the geoid requires the introduction of assumptions concerning the unknown mass distribution between the Earth's surface and the geoid.

In this paper we briefly recapitulate the classical approach to global gravity field determination due to Stokes (1849), Bruns (1878), and Neumann (1887) by formulating the differential/integral relations between gravity disturbance, gravity anomaly, vertical deflections on the one hand and the disturbing potential and the geoidal undulations on the other hand. The representation of the disturbing potential in terms of gravity disturbances, gravity anomalies, and deflections of the vertical are written in terms of well-known integral representations over the geoid. For practical purposes the integrals are replaced by approximate cubature formulas using certain integration weights and knots within a spherical framework. Seen

* Corresponding author, e-mail: freeden@mathematik.uni-kl.de, Phone: +49 631 205 3867, Fax: +49 631 205 4736

from the view of constructive approximation, however, the approximate integration formulas are the essential problem in the spherical framework of determining globally the disturbing potential and the geoidal heights. On the one hand, Weyl's law of equidistribution (cf. [42]) tells us that numerical integration and equidistribution of the nodal points are mathematically equivalent. To get better and better accuracy in numerical integration procedures we thus need denser and denser globally over the whole sphere equidistributed data sets. On the other hand, observations in sufficient data width and quality are only available for certain parts of the Earth's surface, and there are large areas, particularly at sea, where no data are given at all (cf. Figure 1). In fact, it should be noted that terrestrial gravity data coverage now and in the foreseeable future is far from being satisfactory and totally inadequate for the purpose of high precision geoid determination at *global* scale.

Looking at the key aspects in constructive approximation of gravity field determination we are confronted with the following situation: Almost 70% of the Earth's gravity field is smooth. Its modeling by polynomial structures, i.e., spherical harmonics, is the appropriate tool. But what is about the remaining parts that certainly are of more geophysical and geodetic relevance, today? Because of the lack of terrestrial data, trial functions with global support seem to be an inadequate choice for understanding these geoscientifically significant parts in the 'system Earth'. Even more, globally supported approximation structures such as spherical harmonics applied to a heterogeneous data set, e.g., the Earth's gravity anomalies (see Figure 1) also influence large areas in negative way, where a sufficiently high accuracy has already been obtained by a fewer equidistributed number of data.

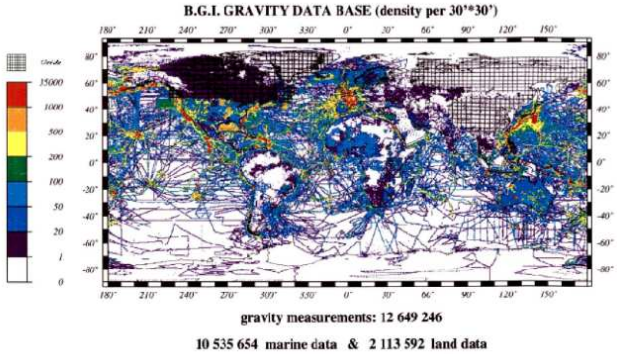

Fig. 1: Data density and distribution of scalar gravity (due to [37]).

Nowadays there are two ways out for modeling the Earth's gravity field: the *first one* is to use spaceborne data (for example, collected by the satellites CHAMP, GRACE, and GOCE). They, indeed give, the opportunity of globally measured and suitably (equi-)distributed data sets (cf. [4], [5], [6], [9]). The critical point, however, is that satellite data are exponentially smoothed with respect to the altitude, hence, they are of lower quality in comparison with terrestrial ones. Satellite-only models based on global datasets are reliable only to a maximum level of accuracy. Nevertheless, the determination of the Earth's gravitational field based on spaceborne observations is a great challange for future geoscientific research (cf. [37]). The *second one* is to use high-precision terrestrial data in their actual heterogeneous distribution and to apply a locally adaptive approximation method. From mathematical point of view this requires a careful analysis involving a 'zooming-in' procedure based on locally supported trial structures such as wavelets.

The layout of this paper is as follows: First we are concerned with the idea of calculating globally reflected integral representations of the disturbing potential by locally oriented 'zooming-in' approximations adaptive to the actual terrestrial data width and distribution. In other words, classical global methods of gravity field determination are formulated in terms of modern local (isotropic) multiscale framework. Essential tools are regularizations of the Green, Neumann, and Stokes integral expressions derived by potential theoretical means. It is shown, that the Green, Neumann, and Stokes kernel, respectively, provide us with so-called Green, Neumann, and Stokes scaling functions. Correspondingly, locally supported wavelets are definable for adaptive (local) multiscale approximation. Finally, the efficiency of our methods is illustrated by some test examples, showing the gravity disturbation caused by plumes in the area of Hawaii and Iceland.

2 Gravity Anomalies and Gravity Potential

The *gravity acceleration (gravity)* w is the resultant of gravitation v and centrifugal acceleration c

$$w = v + c. \tag{1}$$

The centrifugal force c arises as a result of the rotation of the Earth about its axis. We assume here a rotation of constant angular velocity ω about the rotational axis $\varepsilon^3 = (0, 0, 1)^T$, which is further assumed to be fixed with respect to the Earth.

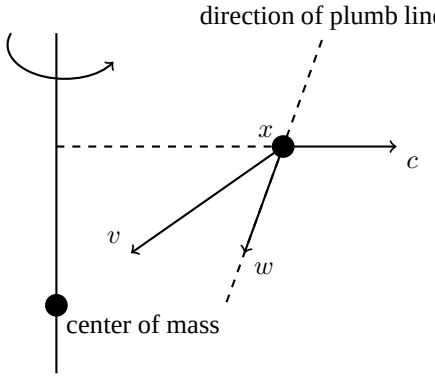

Fig. 2: Gravitation v, centrifugal acceleration c, gravity acceleration w.

The centrifugal acceleration acting on a unit mass is directed outward perpendicularly to the spin axis (see Figure 2). If the ε^3-axis of an Earth's fixed coordinate system coincides with the axis of rotation, then we have

$$c(x) = -\omega^2 \varepsilon^3 \wedge (\varepsilon^3 \wedge x). \tag{2}$$

Using the so–called *centrifugal potential*

$$\begin{aligned} C(x) &= \frac{\omega^2}{2} |\varepsilon^3 \wedge (\varepsilon^3 \wedge x)| \\ &= \frac{\omega^2}{2} \left((x \cdot \varepsilon^1)^2 + (x \cdot \varepsilon^2)^2 \right) \\ &= \frac{\omega^2}{2} (x_1^2 + x_2^2) \end{aligned} \tag{3}$$

we can write $c = \nabla C$. Applying the Laplace operator gives us $\Delta C = 2\omega^2$, thus, the function C is *not* harmonic.
The direction of the gravity w is known as the direction of the *plumb line*, the quantity $g = |w|$ is called the *gravity intensity* (often just (scalar) *gravity*). The *gravity potential of the Earth* can be expressed as the sum of the gravitational potential V and the centrifugal potential C, i.e.,

$$W = V + C. \tag{4}$$

The gravity acceleration w is given by

$$w = \nabla W = \nabla V + \nabla C. \tag{5}$$

The surfaces of constant gravity potential $W(x) = \text{const}$, $x \in \mathbb{R}^3$, are designated as *equipotential (level,* or *geopotential) surfaces of gravity* (for more details see, e.g., [14], [16], [39]).
In an Earth's fixed coordinate system the centrifugal potential C is explicitly known. Hence, the determination of equipotential surfaces of the gravity potential W is strongly related to the knowledge of the gravitational potential V. Equipotential surfaces (see Figure 2) intuitively express the notion of tangential surfaces, as they are normal to the plumb lines given by the direction of the gravity vector.

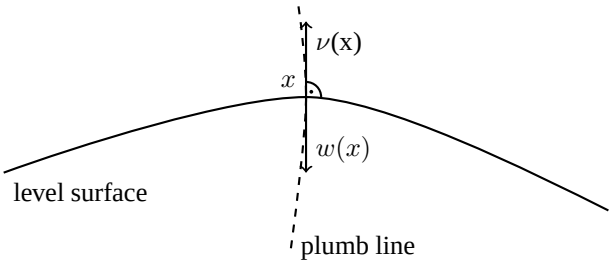

Fig. 3: Level surface and plumb line.

According to the classical Newton Law of Gravitation (1687), knowing the density distribution ρ of a body, the gravitational potential can be computed everywhere in $\mathbb{R}^3$. More explicitly, the gravitational potential V of the Earth's exterior is given by

$$V(x) = G \int_{\text{Earth}} \frac{\rho(y)}{|x-y|}\, dV(y), \quad x \in \mathbb{R}^3 \backslash \text{Earth}, \tag{6}$$

where G is the gravitational constant ($G = 6.6742 \cdot 10^{-11} \text{m}^3\ \text{kg}^{-1}\ \text{s}^{-2}$, for more details see, e.g., [14], [16], [39]). In consequence, the properties of the gravitational potential (6) in the Earth's exterior are easily described as follows:

$$\Delta V(x) = 0,\ x \in \mathbb{R}^3 \backslash \text{Earth}. \tag{7}$$

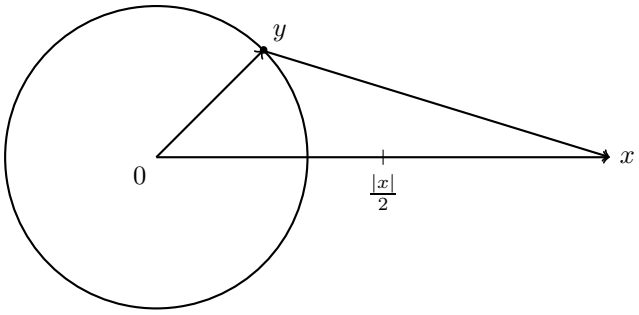

Fig. 4: Regularity at infinity.

Moreover, the gravitational potential V is *regular at infinity*, i.e.,

$$\begin{aligned} |V(x)| &= O\left(\frac{1}{|x|}\right), |x| \to \infty, \\ |\nabla V(x)| &= O\left(\frac{1}{|x|^2}\right),\ |x| \to \infty. \end{aligned} \tag{8}$$

Note that, for suitably large values $|x|$ (see Figure 4), we have $|y| \leq \frac{1}{2}|x|$, hence, $|x-y| \geq ||x|-|y|| \geq \frac{1}{2}|x|$. Clearly, the gravitational field $v = \nabla V$ fulfills the following identities:

$$\text{L} \cdot \nabla V(x) = 0, \quad \nabla \cdot \nabla V(x) = \Delta V(x) = 0, \tag{9}$$

$x \in \mathbb{R}^3 \backslash \text{Earth}$. However, the problem is that in reality the density distribution ρ is very irregular and known only for parts of the upper crust of the Earth. It is actually so that we would like to know it from measuring the gravitational field.

Equipotential surfaces of the gravity potential W allow in general no simple representation. This is the reason why a reference surface, in physical geodesy usually an ellipsoid of revolution, is chosen for the (approximate) construction of the geoid. As a matter of fact, the deviations of the gravity field of the Earth from the normal field of such an ellipsoid are small. The remaining parts of the gravity field are gathered in a so–called *disturbing gravity field* ∇T corresponding to the *disturbing potential* T. Knowing the gravity potential, all equipotential surfaces – including the geoid – are given by an equation of the form $W(x) = \text{const}$. By introducing U as the normal gravity potential corresponding to the ellipsoidal field and T as the disturbing potential (for more details see, e.g., [14], [16], [39]) we are led to a decomposition of the gravity potential in the form

$$W = U + T. \tag{10}$$

In accordance with the Pizzetti concept (see, e.g., [33], [34]) we may assume that

(1) the center of the ellipsoid coincides with the center of the gravity of the Earth,

(2) the difference of the mass of the Earth and the mass of the ellipsoid is zero.

Consequently, following the classical approach (see, e.g., [16], [28]), T is given in such a way that

$$\int_{\Omega_R} T(x)\, d\omega(x) = 0, \tag{11}$$

$$\int_{\Omega_R} T(x)(\varepsilon^k \cdot x)\, d\omega(x) = 0,\ k = 1, 2, 3. \tag{12}$$

A point x of the geoid is projected onto the point y of the ellipsoid by means of the ellipsoidal normal (see Figure 5). The distance between x and y is called the *geoidal height*, or *geoidal undulation*.

The *gravity anomaly vector* is defined as the difference between the gravity vector $w(x)$ and the normal gravity vector $u(y)$, $u = \nabla U$, i.e.,

$$\alpha(x) = w(x) - u(y). \tag{13}$$

It is also possible to form the difference between the vectors w and u at the same point x to get the *gravity disturbance vector*

$$\delta(x) = w(x) - u(x). \tag{14}$$

Of course, several basic mathematical relations between the quantities just mentioned are known. In what follows we only describe heuristically the fundamental relations. We start by observing that the gravity disturbance vector at the point x on the geoid can be written as

$$\delta(x) = w(x) - u(x) = \nabla(W(x) - U(x)) = \nabla T(x). \tag{15}$$

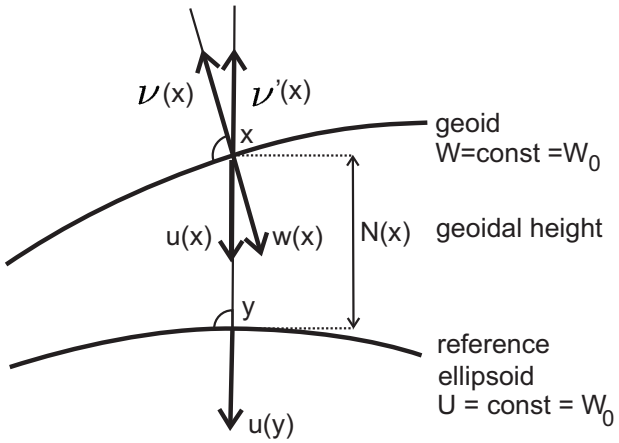

Fig. 5: Illustration of the definition of the gravity anomaly vector $\alpha(x) = w(x) - u(y)$ and the gravity disturbance vector $\delta(x) = w(x) - u(x)$.

Expanding the potential U at x according to Taylor's theorem and truncating the series at the linear term we get

$$U(x) \doteq U(y) + \frac{\partial U}{\partial \nu'}(y) N(x) \tag{16}$$

($\doteq$ means approximation in linearized sense). Here, $\nu'(y)$ is the ellipsoidal normal at y, i.e., $\nu'(y) = -u(y)/\gamma(y)$, $\gamma(y) = |u(y)|$, and the geoid undulation $N(x)$, as indicated in Figure 5, is the aforementioned distance between x and y, i.e., between the geoid and the reference ellipsoid. Using

$$\begin{aligned} \gamma(y) &= |u(y)| = -\nu'(y) \cdot u(y) \\ &= -\nu'(y) \cdot \nabla U(y) = -\frac{\partial U}{\partial \nu'}(y) \end{aligned} \tag{17}$$

we arrive at

$$\begin{aligned} N(x) &= \frac{T(x) - (W(x) - U(y))}{|u(y)|} \\ &= \frac{T(x) - (W(x) - U(y))}{\gamma(y)}. \end{aligned} \tag{18}$$

Observing $U(y) = W(x) = \text{const} = W_0$ we obtain the so-called *Bruns' formula* (cf. [2])

$$N(x) = \frac{T(x)}{|u(y)|} = \frac{T(x)}{\gamma(y)}. \tag{19}$$

It should be noted that Bruns' formula (19) relates the physical quantity T to the geometric quantity N.

In what follows we are interested in introducing the deflections of the vertical of the gravity disturbing potential T. For this purpose, let us consider the vector field $\nu(x) = -w(x)/|w(x)|$. This gives us the identity (with $g(x) = |w(x)|$ and $\gamma(x) = |u(x)|$)

$$w(x) = \nabla W(x) = -|w(x)|\ \nu(x) = -g(x)\nu(x). \tag{20}$$

Furthermore, we have

$$u(x) = \nabla U(x) = -|u(x)|\ \nu'(x) = -\gamma(x)\nu'(x). \tag{21}$$

The *deflection of the vertical* $\Theta(x)$ at the point x on the geoid is defined to be the angular (i.e., tangential) difference between the directions $\nu(x)$ and $\nu'(x)$, i.e., the plumb line and the ellipsoidal normal through the same point:

$$\Theta(x) = \nu(x) - \nu'(x) - ((\nu(x) - \nu'(x)) \cdot \nu(x))\, \nu(x). \tag{22}$$

Clearly, because of (22), $\Theta(x)$ is orthogonal to $\nu(x)$, i.e., $\Theta(x) \cdot \nu(x) = 0$. Since the plumb lines are orthogonal to the level surfaces of the geoid and the ellipsoid, respectively, the deflections of the vertical give briefly spoken a measure of the gradient of the level surfaces. This aspect will be described in more detail below: From (20) we obtain, in connection with (22),

$$\begin{aligned} w(x) &= \nabla W(x) \\ &= -|w(x)|\,(\Theta(x) + \nu'(x) + ((\nu(x) - \nu'(x)) \cdot \nu(x))\nu(x))\,. \end{aligned} \tag{23}$$

Altogether we get for the gravity disturbance vector

$$\begin{aligned} w(x) - u(x) &= \nabla T(x) \\ &= -|w(x)|\,(\Theta(x) + ((\nu(x) - \nu'(x)) \cdot \nu(x))\,\nu(x)) \\ &- (|w(x)| - |u(x)|)\,\nu'(x). \end{aligned} \tag{24}$$

The magnitude

$$D(x) = |w(x)| - |u(x)| = g(x) - \gamma(x) \tag{25}$$

is called the *gravity disturbance*, while

$$A(x) = |w(x)| - |u(y)| = g(x) - \gamma(y) \tag{26}$$

is called the *gravity anomaly*.

Since the vector $\nu(x) - \nu'(x)$ is (almost) orthogonal to $\nu'(x)$, it can be neglected in (24). Hence, it follows that

$$\begin{aligned} w(x) - u(x) &= \nabla T(x) \\ &\doteq -|w(x)|\Theta(x) - (|w(x)| - |u(x)|)\,\nu'(x). \end{aligned} \tag{27}$$

The gradient $\nabla T(x)$ can be split into a normal part (pointing into the direction of $\nu(x)$) and an angular (tangential) part (characterized by the surface gradient ∇^*). It follows that

$$\nabla T(x) = \frac{\partial T}{\partial \nu}(x)\nu(x) + \frac{1}{|x|}\nabla^* T(x). \tag{28}$$

By comparison of (27) and (28) we therefore obtain

$$D(x) = g(x) - \gamma(x) = |w(x)| - |u(x)| = -\frac{\partial T}{\partial \nu'}(x), \tag{29}$$

i.e., the gravity disturbance, beside being the difference in magnitude of the actual and the normal gravity vector, is also the normal component of the gravity disturbance vector. In addition, we are led to the angular, i.e., (tangential) differential equation

$$\frac{1}{|x|}\nabla^* T(x) = -|w(x)|\ \Theta(x). \tag{30}$$

Since $|\Theta(x)|$ is a small quantity, it may be (without loss of precision) multiplied either by $-|w(x)|$ or by $-|u(x)|$, i.e., $-g(x)$ or by $-\gamma(x)$.

The reference ellipsoid deviates from a sphere only by quantities of the order of the flattening. Therefore, in numerical calculations, if we treat the reference ellipsoid as a sphere $\Omega_R = \{x \in \mathbb{R}^3 \mid x = R\xi,\ R = |x|,\ \xi \in \Omega\}$, $\Omega = \Omega_1$, (with mean radius R as defined by, e.g., [16], [17]) this may cause a relative error of the same order (for more details the reader is referred to standard textbooks of physical geodesy (e.g., [16], [17]). If this error is permissible, we are allowed to replace $|u(R\xi)|$ by its spherical approximation GM/R^2 such that

$$\nabla^*_\xi T(R\xi) = -\frac{GM}{R}\Theta(R\xi), \tag{31}$$

where G is the gravitational constant and M is the constant of the mass. By virtue of Bruns' formula we finally find

$$\frac{GM}{R^2}\nabla^*_\xi N(R\xi) = -\frac{GM}{R}\Theta(R\xi), \quad \xi \in \Omega, \tag{32}$$

i.e.,

$$\nabla^*_\xi N(R\xi) = -R\,\Theta(R\xi), \quad \xi \in \Omega. \tag{33}$$

In other words, the knowledge of the geoid undulations allows the determination of the deflections of the vertical by taking the surface gradient on the unit sphere.

From the identity (29) it follows that

$$\begin{aligned} -\frac{\partial T}{\partial \nu'}(x) = D(x) &= |w(x)| - \gamma(x) \\ &\doteq |w(x)| - \gamma(y) - \frac{\partial \gamma}{\partial \nu'}(y)\ N(x) \\ &= A(x) - \frac{\partial \gamma}{\partial \nu'}(y)\ N(x), \end{aligned} \tag{34}$$

where A represents the scalar gravity anomaly as defined by (26). Observing Bruns' formula (19) we get

$$A(x) = -\frac{\partial T}{\partial \nu'}(x) + \frac{1}{\gamma(y)}\frac{\partial \gamma}{\partial \nu'}(y)\ T(x). \tag{35}$$

In well-known *spherical approximation* we have (see, e.g., [16])

$$\gamma(y) = |u(y)| = \frac{GM}{|y|^2}, \tag{36}$$

$$\frac{\partial \gamma}{\partial \nu'}(y) = \frac{y}{|y|}\cdot\nabla\gamma(y) = -2\frac{GM}{|y|^3}, \tag{37}$$

and

$$\frac{1}{\gamma(y)}\frac{\partial \gamma}{\partial \nu'}(y) = -\frac{2}{|y|}. \tag{38}$$

This leads us to the basic relations

$$-D(x) = \frac{x}{|x|}\cdot\nabla T(x), \quad x \in \Omega_R, \tag{39}$$

and

$$-A(x) = \frac{x}{|x|}\cdot\nabla T(x) + \frac{2}{|x|}T(x), \quad x \in \Omega_R, \tag{40}$$

as so-called *fundamental equations of physical geodesy*.

In the sense of physical geodesy (cf., e.g., [16]), the meaning of the spherical approximation should be carefully kept in mind. It is used only for expressions relating to small quantities of the disturbing potential, the geoidal undulations, the gravity disturbances, the gravity anomalies, etc. Actually, in all geodetic approaches, the reference surface will never be understood to be a sphere in any geometrical sense, but it always is an ellipsoid (see [1] for more details). However, as the

flattening of this ellipsoid is very small, the ellipsoidal formulas are expandable into Taylor series in terms of the flattening, and then all terms containing higher order expressions of the flattening may be neglected. In this way together with suitable pre-reduction processes of gravity formulas are obtained that are rigorously valid for the sphere.

It should be mentioned that, in the gravity disturbances and gravity anomalies all significantly tectonic processes become visible (see Figures 8, 12). In accordance with Newton's law the gravity disturbances and gravity anomalies permit the conclusion of an irregular density distribution inside the Earth. Unfortunately, gravity anomalies do not determine uniquely the interior density distribution of the Earth. Geoid undulations are the measure of the pertubations in the hydrostatic equilibrium. They do not show essential correlations to the distribution of the continents (see Figure 13).

3 Modeling of Gravity Disturbances, Gravity Anomalies, and Deflections of the Vertical by Haar Wavelets

Wavelets enable us to break up functions into many simple pieces at different scales and positions. Thus, three features are incorporated in this way of thinking about geodetically relevant wavelets: Wavelets are 'building blocks' that enable fast decorrelation of gravity data. Whenever we are interested in a multiscale analysis of local 'fine-structure' within a smooth(er) global structure, wavelets are the mathematical tools of choice. They are the natural means for investigating signals as, e.g., the gravity disturbance or the gravity anomaly, in small bounded areas out of a global context by the power of a 'zooming-in' process.

The wavelets are constructed by use of scaling functions (in the jargon of functional analysis, Dirac sequences) showing the property of tending to the Dirac kernel δ (understood in distributional sense) given by

$$\delta(\xi \cdot \eta) = \sum_{n=0}^{\infty} \frac{2n+1}{4\pi} P_n(\xi \cdot \eta). \tag{41}$$

Multiscale modeling can be performed in frequency domain based on specific features within a spherical harmonic context (see, e.g., [7], [9], [10]). But it can also be done exclusively in space domain, and this is the approach that should be presented here.

More formally, let $\{H^{\rho_j}\}_{j\in\mathbb{N}_0}$ be a Dirac family of L^2-scaling functions such that H^{ρ_j} tends to the Dirac kernel as the 'scale' j tends to infinity. Then the convolution

$$F^{\rho_j}(\xi) = \int_{\Omega} H^{\rho_j}(\xi \cdot \eta) F(\eta)\, d\omega(\eta), \quad F \in \mathrm{L}^2(\Omega), \tag{42}$$

is a j-level approximation of F, i.e., a low-pass filtered version of F. Moreover, the approximate identity

$$\lim_{j\to\infty} \|F^{\rho_j} - F\|_{\mathrm{L}^2(\Omega)} = 0 \tag{43}$$

can be guaranteed. In other words, as the scaling functions H^{ρ_j} converge to the Dirac functional, the functions F^{ρ_j} tend to the limit function

$$F(\xi) = \int_{\Omega} \delta(\xi \cdot \eta) F(\eta)\, d\omega(\eta), \quad F \in \mathrm{L}^2(\Omega), \tag{44}$$

(understood in L^2-topology).
The wavelets $\{(WH)^{\rho_j}\}_{j\in\mathbb{N}_0}$ are nothing else than differences of two consecutive scaling functions,

$$(WH)^{\rho_j} = H^{\rho_{j+1}} - H^{\rho_j}, \quad j \in \mathbb{N}_0, \tag{45}$$

such that the detail information in $F^{\rho_{j+1}}$ that is not included in F^{ρ_j} is provided by

$$(WF)^{\rho_j}(\xi) = \int_{\Omega} (WH)^{\rho_j}(\xi \cdot \eta) F(\eta)\, d\omega(\eta), \quad F \in \mathrm{L}^2(\Omega). \tag{46}$$

In consequence, the multiscale process is determined by two parameters, viz. the scale j characterizing the 'zooming-in' width and the position ξ indicating the 'zooming-in' center. With increasing scale j, the wavelets $\{(WH)^{\rho_j}\}_{j\in\mathbb{N}_0}$ extract more and more detailed information out of F.

Clearly, there are millions of scaling functions generating difference wavelet functions. Of particular economy and efficiency for purposes of numerical computation, however, are wavelet kernels given in terms of elementary functions and

possessing a local support. But also locally supported trial functions are nothing new, having been discussed already by Haar (1910) in one–dimensional Euclidean theory (see [15]). The spherical Haar wavelet is zero outside a small spherical cap. In fact, Haar wavelets represent an ideal choice for locally oriented 'zooming-in'-approximation of geodetic quantities, since signal values outside their spherical support are not taken into account at all. Consequently, local improvements can be guaranteed for smaller and smaller local parts with increase in accuracy, but without any deterioration of the approximated signal in all other parts outside. Note that the size of the local support depends on the scale j of the wavelet H^{ρ_j}, i.e., with increasing scale j its diameter decreases. This is the reason why the wavelet concept allows an ideal 'zooming-in' process to local (high frequency) phenomena.

The apparatus of (smoothed) Haar scaling and wavelet functions should be concretized: Let $\{\rho_j\}_{j\in\mathbb{N}_0}$ be a sequence with $\lim_{j\to\infty}\rho_j = 0$ (for example, $\rho_j = 2^{-j}$ or $\rho_j = 1-\cos 2^{-j}\pi$). The *(smoothed) Haar scaling functions* $\{H^{\rho_j}\}_{j\in\mathbb{N}_0}$, are defined by

$$H^{\rho_j}(\xi\cdot\eta) \quad = \quad \begin{cases} 0, & \rho_j < 1-\xi\cdot\eta \le 2 \\ (\frac{k+1}{2\pi})\rho_j^{-(k+1)}(\xi\cdot\eta-1+\rho_j)^k, & 0 \le 1-\xi\cdot\eta \le \rho_j \end{cases}$$

where ξ,η are elements of the unit sphere Ω and k denotes a (fixed) polynomial degree. Note, that the smoothed *Haar scaling function* H^{ρ_j} occurs to be rotationally invariant, i.e., it is a so-called zonal function. Correspondingly, the *smoothed Haar wavelets* $(WH)^{\rho_j}$, are defined as the difference of two consecutive scaling functions, i.e.

$$(WH)^{\rho_j} = H^{\rho_{j+1}} - H^{\rho_j}, \quad j\in\mathbb{N}_0. \tag{47}$$

Due to its definition as zonal function the Haar wavelet has a spherical cap as local support on Ω, i.e.,

$$\mathcal{S}^{\rho_j}(\xi) = \operatorname{supp}(WH)^{\rho_j}(\xi\cdot) = \{\eta\in\Omega | 1-\xi\cdot\eta\le\rho_j\}. \tag{48}$$

Explicitly written out, the Haar wavelets (see Figure 7) read as follows

$$(WH)^{\rho_j}(\xi\cdot\eta) \quad = \quad \begin{cases} 0, & \rho_j < 1-\xi\cdot\eta \le 2 \\ -(\frac{k+1}{2\pi})\rho_j^{-(k+1)}(\xi\cdot\eta-1+\rho_j)^k, & \rho_{j+1} < 1-\xi\cdot\eta \le \rho_j \\ (\frac{k+1}{2\pi})\left(\rho_{j+1}^{-(k+1)}(\xi\cdot\eta-1+\rho_{j+1})^k\right. & \\ \left.-\rho_j^{-(k+1)}(\xi\cdot\eta-1+\rho_j)^k\right), & 0 \le 1-\xi\cdot\eta \le \rho_{j+1}. \end{cases}$$

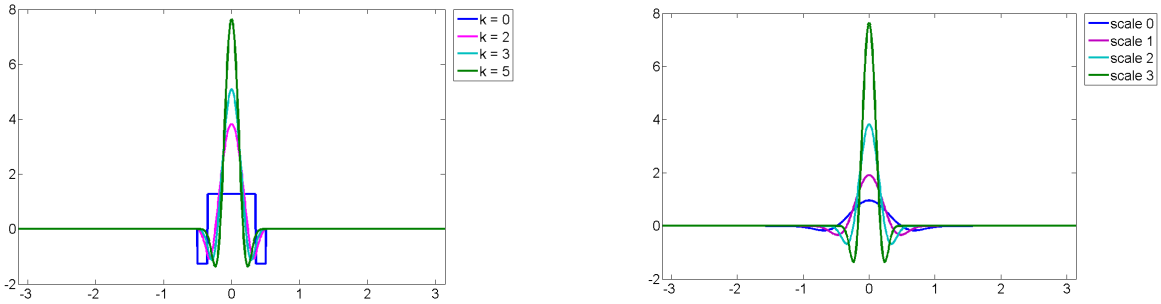

scale $j=3$, $k=0,2,3,5$ scale $j=0,1,2,3$, $k=5$

Fig. 6: Illustration of the smoothed Haar wavelets ($\rho_j = 2^{-j}$).

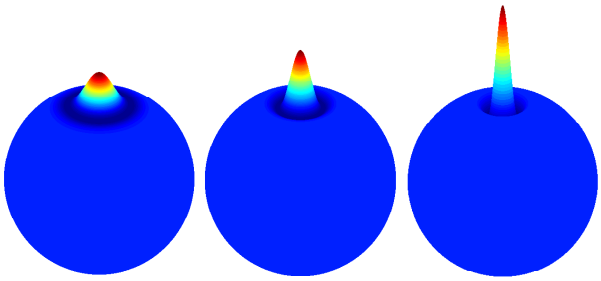

Fig. 7: Illustration of the smoothed Haar wavelet on the sphere ($\rho_j = 2^{-j}$, $j=2,3,4$, $k=5$).

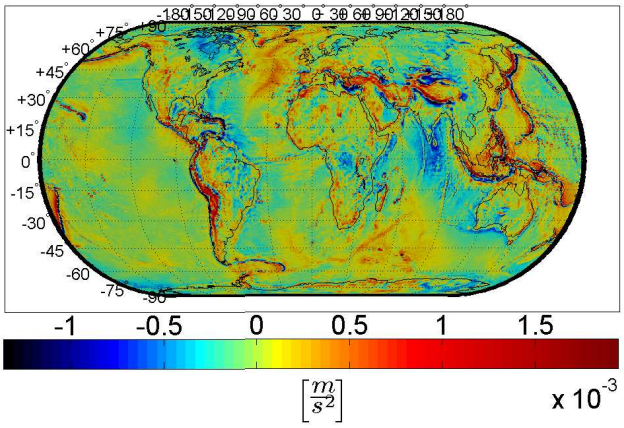

Fig. 8: The gravity disturbance D.

Note, that the degree k regulates the order of differentiability, i.e., the chosen smoothness property of the Haar kernel.

4 Modeling of the Disturbing Potential from Gravity Disturbances by Neumann Wavelets

Since the disturbing potential T (see Figure 9) is a harmonic function in the exterior Ω_R^{ext} of the sphere Ω_R around the origin with a radius R, we are confronted with a boundary value problem of potential theory to determine T in Ω_R^{ext} from prescribed gravity disturbance D or gravity anomaly A, respectively. Moreover, it should be noted that, at the present state of practice, much more gravity anomalies are available than gravity disturbances. In future, because of GPS-technology, it may be expected that the gravity disturbances become more important than the gravity anomalies (for more details see, e.g., [17]). This is the reason why both problems will be discussed here.

The determination of the disturbing potential T in the outer space Ω_R^{ext} of Ω_R, from known gravity disturbances D on Ω_R (see Figure 8), leads us to the Neumann (type) boundary value problem:

(Modified) Exterior Neumann Problem (ENP): We are given $D \in \mathrm{C}^{(0)}(\Omega_R)$ with

$$\int_{\Omega_R} D(x)\, d\omega(x) = 0 \tag{49}$$

and

$$\int_{\Omega_R} D(x)(\varepsilon^k \cdot x)\, d\omega(x) = 0, \quad k = 1,2,3. \tag{50}$$

Then the function $T : \overline{\Omega_R^{ext}} \to \mathbb{R}$ given by

$$T(x) = \frac{1}{4\pi R} \int_{\Omega_R} N(x,y) D(y)\, d\omega(y) \tag{51}$$

with the *Neumann kernel function* $N : \overline{\Omega_R^{\text{ext}}} \times \overline{\Omega_R^{\text{ext}}} \to \mathbb{R}$

$$N(x,y) = \frac{2R}{|x-y|} + \ln\left(\frac{|x| + |x-y| - R}{|x| + |x-y| + R}\right) \tag{52}$$

is the unique solution of the exterior Neumann boundary value problem:

(i) T is continuously differentiable in $\overline{\Omega_R^{ext}}$ and twice continuously differentiable in Ω_R^{ext}, i.e., $T \in \mathrm{C}^{(1)}(\overline{\Omega_R^{ext}}) \cap \mathrm{C}^{(2)}(\Omega_R^{\text{ext}})$,

(ii) T is harmonic in Ω_R^{ext}, i.e., $\Delta T = 0$ in Ω_R^{ext},

(iii) T is regular at infinity, i.e., $|T(x)| = O\left(\frac{1}{|x|}\right), |\nabla T(x)| = O\left(\frac{1}{|x|^2}\right)$ as $|x| \to \infty$,

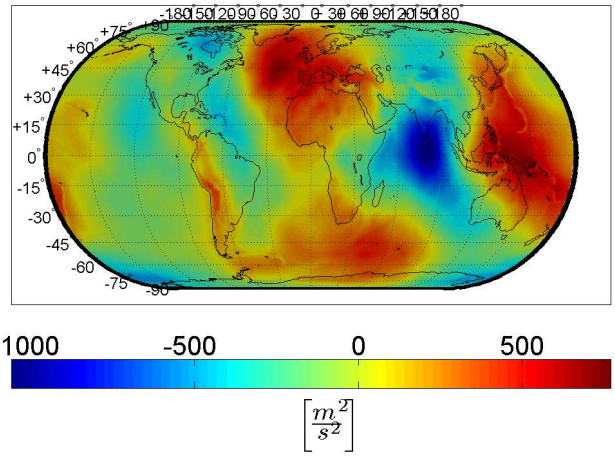

Fig. 9: The disturbing potential T.

(iv) $\int_{\Omega_R} T(x)\, d\omega(x) = 0$

and

$\int_{\Omega_R} T(x)(\varepsilon^k \cdot x)\, d\omega(x) = 0, k = 1, 2, 3.$

(v) $-\frac{x}{|x|} \cdot \nabla T(x) = D(x), \quad x \in \Omega_R.$

For points $x, y \in \Omega_R$ we (formally) get the so–called *Neumann formula* which is an improper integral over Ω_R

$$T\left(\frac{Rx}{|x|}\right) = \frac{1}{4\pi R} \int_{\Omega_R} \left(\frac{\sqrt{2}}{\sqrt{1 - \frac{x}{|x|} \cdot \frac{y}{|y|}}} + \ln \left(\frac{\sqrt{2 - 2\frac{x}{|x|} \cdot \frac{y}{|y|}}}{2 + \sqrt{2 - 2\frac{x}{|x|} \cdot \frac{y}{|y|}}} \right) \right) D\left(\frac{Ry}{|y|}\right)\, d\omega(y).$$

Note that the surface integral (53) indeed has to be extended over the whole surface. In accordance with our approach it is valid under the following assumptions: (i) the mass within the reference ellipsoid is equal to the mass of the Earth, (ii) the potential of the geoid and the reference ellipsoid are equal, (iii) the center of the reference ellipsoid is coincident with the center of the Earth, (iv) there are no masses outside, (v) the approximation is simplyfied in spherical sense.

The identity (53) formulated in an equivalent way over the unit sphere Ω yields

$$T(R\xi) = \frac{R}{4\pi} \int_{\Omega} N(\xi \cdot \eta) D(R\eta)\, d\omega(\eta), \quad \xi \in \Omega \tag{53}$$

where the *Neumann kernel* is given by

$$N(\xi \cdot \eta) = \frac{\sqrt{2}}{\sqrt{1 - \xi \cdot \eta}} - \ln\left(1 + \frac{\sqrt{2}}{\sqrt{1 - \xi \cdot \eta}}\right), \; 1 - \xi \cdot \eta \neq 0. \tag{54}$$

Note that

$$N(R\xi, R\eta) = N(\xi \cdot \eta), \quad \xi, \eta \in \Omega. \tag{55}$$

The essential idea now is that the improper integral (53) can be regularized, e.g., by replacing the zonal kernel

$$S(\xi \cdot \eta) = \frac{\sqrt{2}}{\sqrt{1 - \xi \cdot \eta}}, \qquad 1 - \xi \cdot \eta \neq 0, \tag{56}$$

by the space–regularized zonal kernel (see Figure 10)

$$S^\rho(\xi \cdot \eta) = \begin{cases} \frac{R}{\rho}\left(3 - \frac{2R^2}{\rho^2}(1 - \xi \cdot \eta)\right), & 0 \leq 1 - \xi \cdot \eta \leq \frac{\rho^2}{2R^2} \\ \frac{\sqrt{2}}{\sqrt{1 - \xi \cdot \eta}}, & \frac{\rho^2}{2R^2} < 1 - \xi \cdot \eta \leq 2. \end{cases}$$

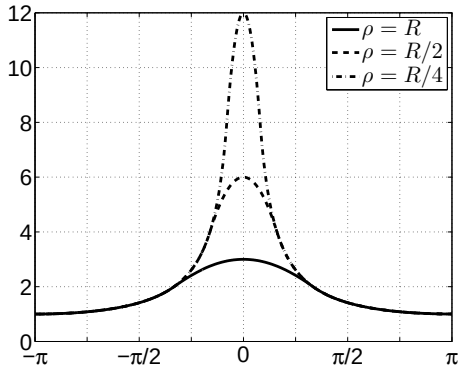

Fig. 10: The kernel $\vartheta \mapsto S^\rho(\cos\vartheta)$ (57) for several ρ.

This leads us to the following space–regularized representation of the disturbing potential (see Figure 9) in terms of known gravity disturbances on Ω_R

$$\begin{aligned} T^\rho(R\xi) &= \frac{R}{4\pi} \int\limits_{1-\xi\cdot\eta > \frac{\rho^2}{2R^2}} \frac{\sqrt{2}}{\sqrt{1-\xi\cdot\eta}} D(R\eta)\, d\omega(\eta) \\ &- \frac{R}{4\pi} \int\limits_{1-\xi\cdot\eta > \frac{\rho^2}{2R^2}} \ln\left(1+\frac{\sqrt{2}}{\sqrt{1-\xi\cdot\eta}}\right) D(R\eta)\, d\omega(\eta) \\ &+ \frac{R}{4\pi} \int\limits_{1-\xi\cdot\eta \le \frac{\rho^2}{2R^2}} \frac{R}{\rho}\left(3-\frac{2R^2}{\rho^2}(1-\xi\cdot\eta)\right) D(R\eta)\, d\omega(\eta) \\ &- \frac{R}{4\pi} \int\limits_{1-\xi\cdot\eta \le \frac{\rho^2}{2R^2}} \ln\left(1+\frac{R}{\rho}\left(3-\frac{2R^2}{\rho^2}(1-\xi\cdot\eta)\right)\right) D(R\eta)\, d\omega(\eta). \end{aligned}$$

In other words, a low–pass filtered version of T is given by

$$T^\rho(R\xi) = \frac{R}{4\pi}\int_\Omega N^\rho(\xi\cdot\eta) D(R\eta)\, d\omega(\eta), \tag{57}$$

where the regularized Neumann kernel reads as follows

$$N^\rho(\xi\cdot\eta) = S^\rho(\xi\cdot\eta) - \ln(1+S^\rho(\xi\cdot\eta)), \quad \xi,\eta\in\Omega. \tag{58}$$

Note that $t \mapsto S^\rho(t), t\in[-1,1]$, given by

$$S^\rho(t) = \begin{cases} \dfrac{R}{\rho}\left(3-\dfrac{2R^2}{\rho^2}(1-t)\right), & 0 \le 1-t \le \frac{\rho^2}{2R^2} \\ \dfrac{\sqrt{2}}{\sqrt{1-t}}, & \frac{\rho^2}{2R^2} < 1-t \le 2 \end{cases}$$

is continuously differentiable. Moreover, we have (cf. Figure 11)

$$S\left(1-\frac{\rho^2}{2R^2}\right) = S^\rho\left(1-\frac{\rho^2}{2R^2}\right) \tag{59}$$

and

$$S'\left(1-\frac{\rho^2}{2R^2}\right) = (S^\rho)'\left(1-\frac{\rho^2}{2R^2}\right). \tag{60}$$

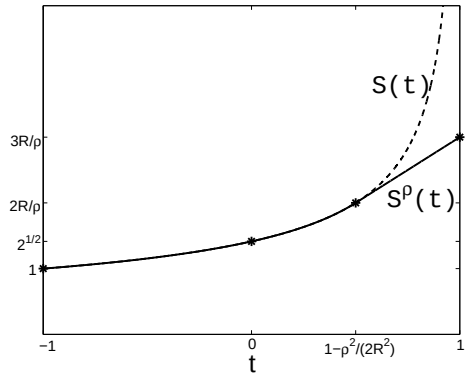

Fig. 11: The functions S and S^ρ on the intervall $[-1,1)$ and $[-1,1]$, respectively.

Furthermore, S and S^ρ are monotonically increasing with

$$S(t) \geq S^\rho(t) \geq 1 \tag{61}$$

for all $t \in [-1,1)$. Furthermore,

$$S(t) - S^\rho(t) \quad = \quad \begin{cases} \frac{\sqrt{2}}{\sqrt{1-t}} - \frac{R}{\rho}\left(3 - \frac{2R^2}{\rho^2}(1-t)\right), & 0 < 1-t \leq \frac{\rho^2}{2R^2} \\ 0, & \frac{\rho^2}{2R^2} < 1-t \leq 2. \end{cases}$$

Elementary calculations give

$$\begin{aligned} \int_{-1}^{+1} |S(t) - S^\rho(t)| \; dt &= \int_{1-\frac{\rho^2}{2R^2}}^{1} (S(t) - S^\rho(t)) \; dt \\ &= O(\rho) \end{aligned} \tag{62}$$

as $\rho \to 0$, hence, it follows that

$$\lim_{j\to\infty} \int_{-1}^{+1} |S(t) - S^{\rho_j}(t)| \, dt = 0. \tag{63}$$

Observing the properties of the functions S and S^ρ we find

$$|\ln(S(t)) - \ln(S^\rho(t))| \leq |S(t) - S^\rho(t)| \tag{64}$$

and

$$|\ln(1+S(t)) - \ln(1+S^\rho(t))| \leq \frac{1}{2} |S(t) - S^\rho(t)| \, . \tag{65}$$

Consequently, we have

$$\int_\Omega |\ln(1+S(\xi\cdot\eta)) - \ln(1+S^\rho(\xi\cdot\eta))| \; d\omega(\eta) = O(\rho). \tag{66}$$

Since $D(R\cdot) : \Omega \to \mathbb{R}$ is continuous and, therefore, uniformly bounded on Ω_R, we finally obtain in connection with (66)

$$\lim_{j\to\infty} \sup_{\xi\in\mathcal{T}} |T(R\xi) - T^{\rho_j}(R\xi)| \quad = \quad \lim_{j\to\infty} \sup_{\xi\in\mathcal{T}} \frac{R}{4\pi} \left| \int_\Omega (N(\xi\cdot\eta) - N^{\rho_j}(\xi\cdot\eta)) D(R\eta) \; d\omega(\eta) \right| = 0$$

for all subsets $\mathcal{T} \subset \Omega$, provided that $\{\rho_j\}_{j\in\mathbb{N}_0}$ is a sequence with $\lim\limits_{j\to\infty} \rho_j = 0$.

Corresponding to the sequence $\{N^{\rho_j}\}_{j\in\mathbb{N}_0}$ of *Neumann scaling functions* N^{ρ_j} given by

$$N^{\rho_j}(\xi\cdot\eta) \quad = \quad \begin{cases} S^{\rho_j}(\xi\cdot\eta) - \ln(1+S^{\rho_j}(\xi\cdot\eta)), & 0 \leq 1-\xi\cdot\eta \leq \frac{\rho_j^2}{2R^2} \\ S(\xi\cdot\eta) - \ln(1+S(\xi\cdot\eta)), & \frac{\rho_j^2}{2R^2} < 1-\xi\cdot\eta \leq 2, \end{cases}$$

we introduce the sequence $\{(WN)^{\rho_j}\}_{j\in\mathbb{N}_0}$ of *Neumann wavelets* given by

$$(WN)^{\rho_j}(\xi\cdot\eta) = N^{\rho_{j+1}}(\xi\cdot\eta) - N^{\rho_j}(\xi\cdot\eta), \quad \xi,\eta\in\Omega. \tag{67}$$

Written out their representations read as follows

$$(WN)^{\rho_j}(\xi\cdot\eta) \;=\; \begin{cases} S^{\rho_{j+1}}(\xi\cdot\eta) - \ln(1+S^{\rho_{j+1}}(\xi\cdot\eta)) & \\ -S^{\rho_j}(\xi\cdot\eta) + \ln(1+S^{\rho_j}(\xi\cdot\eta)), & 0\le 1-\xi\cdot\eta\le\frac{\rho_{j+1}^2}{2R^2} \\ S(\xi\cdot\eta) - \ln(1+S(\xi\cdot\eta)) & \\ -S^{\rho_j}(\xi\cdot\eta) + \ln(1+S^{\rho_j}(\xi\cdot\eta)), & \frac{\rho_{j+1}^2}{2R^2} < 1-\xi\cdot\eta\le\frac{\rho_j^2}{2R^2} \\ 0, & \frac{\rho_j^2}{2R^2} < 1-\xi\cdot\eta\le 2. \end{cases}$$

In other words, $(\xi,\eta)\mapsto(WN)^{\rho_j}(\xi\cdot\eta)$, $\xi,\eta\in\Omega$, is a zonal function (dependent only on the scalar product $\xi\cdot\eta$ of two unit vectors ξ and η). The function has the local support

$$\mathcal{S}^{\rho_j}(\xi) = \text{supp}\,(WN)^{\rho_j}(\xi\cdot) = \left\{\eta\in\Omega | 1-\xi\cdot\eta\le\frac{\rho_j^2}{2R^2}\right\}. \tag{68}$$

Clearly, for increasing j the local support of the Neumann wavelets becomes smaller and smaller such that a 'zooming-in' calculation can be assured for locally distributed gravity disturbances (without globally violating Weyl's law of equidistribution).

5 Modeling of the Disturbing Potential from Gravity Anomalies by Stokes Wavelets

The determination of the disturbing potential T on Ω_R^{ext} from known gravity anomalies A on Ω_R (see Figure 12) leads us to the Stokes boundary value problem.

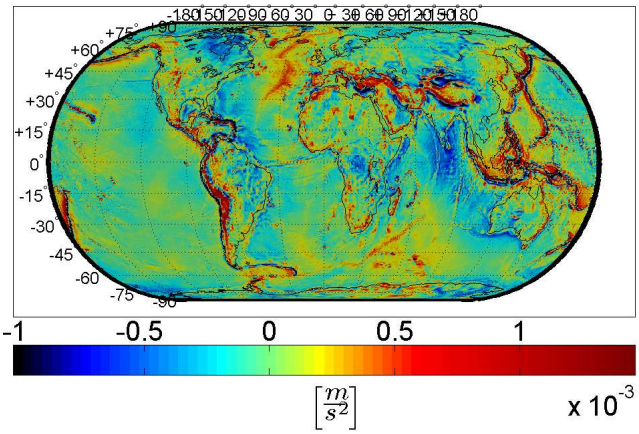

Fig. 12: Gravity anomalies A.

Exterior Stokes Problem (ESP):
We are given $A\in \mathrm{C}^{(0)}(\Omega_R)$ with

$$\int_{\Omega_R} A(x)\,d\omega(x) = 0 \tag{69}$$

and

$$\int_{\Omega_R} A(x)(\varepsilon^k\cdot x)\,d\omega(x) = 0, \quad k=1,2,3. \tag{70}$$

Then the function $T : \overline{\Omega_R^{ext}} \to \mathbb{R}$ given by

$$T(x) = \frac{1}{4\pi R} \int_{\Omega_R} A(y) St(x,y)\, d\omega(y) \tag{71}$$

with the *Stokes kernel function (briefly called Stokes kernel)*

$$\begin{aligned} St(x,y) &= \frac{R}{|x|} + \frac{2R}{|x-y|} - \frac{5R^2}{|x|^2}\frac{x}{|x|}\cdot\frac{y}{|y|} - \frac{3R}{|x|^2}|x-y| \\ &\quad - 3\frac{R^2}{|x|^2}\frac{x}{|x|}\cdot\frac{y}{|y|}\ln\left(\frac{|x| - R\frac{x}{|x|}\cdot\frac{y}{|y|} + |x-y|}{2|x|}\right) \end{aligned} \tag{72}$$

is the unique solution of the exterior Stokes boundary value problem (see, e.g., [16]):

(i) T is continuously differentiable in $\overline{\Omega_R^{ext}}$ and twice continuously differentiable in $\Omega_R^{\rm ext}$, i.e., $T \in \mathrm{C}^{(1)}(\overline{\Omega_R^{ext}}) \cap \mathrm{C}^{(2)}(\Omega_R^{\rm ext})$,

(ii) T is harmonic in $\Omega_R^{\rm ext}$, i.e., $\Delta T = 0$ in $\Omega_R^{\rm ext}$,

(iii) T is regular at infinity,

(iv) $\int_{\Omega_R} T(x)\, d\omega(x) = 0$, and $\int_{\Omega_R} T(x)(\varepsilon^k \cdot x)\, d\omega(x) = 0, \quad k = 1,2,3,$

(v) $-\frac{x}{|x|}\cdot\nabla T(x) - \frac{2}{|x|}T(x) = A(x), \quad x \in \Omega_R.$

For points $x = R\xi,\ y = R\eta \in \Omega_R$ we (formally) get an analogue to the Neumann formula, called *Stokes' formula*, which again represents an improper integral over Ω_R

$$T(R\xi) = \frac{1}{4\pi R}\int_{\Omega_R} St(R\xi, R\eta) A(R\eta)\, d\omega(R\eta). \tag{73}$$

Equivalently we have

$$T(R\xi) = \frac{R}{4\pi}\int_{\Omega} St(\xi\cdot\eta) A(R\eta)\, d\omega(\eta), \tag{74}$$

where

$$St(\xi\cdot\eta) = S(\xi\cdot\eta) - 6(S(\xi\cdot\eta))^{-1} + 1 - 5\xi\cdot\eta - 3\xi\cdot\eta\ln\left(\frac{1}{S(\xi\cdot\eta)} + \frac{1}{(S(\xi\cdot\eta))^2}\right).$$

Note that

$$St(R\xi, R\eta) = St(\xi\cdot\eta), \quad \xi,\eta \in \Omega. \tag{75}$$

From Bruns' formula

$$N(R\xi) = T(R\xi)\frac{R^2}{GM} \tag{76}$$

we get the geodial undulations (see Figure 13).

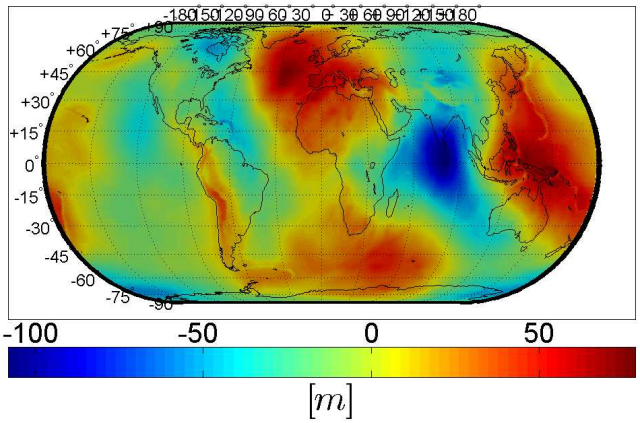

Fig. 13: Geoidal undulations N.

Again, the improper integral (74) can be regularized, e.g., by replacing the zonal kernel S (see (56)) by the space–regularized zonal kernel S^ρ (see (57)).

In fact, the regularization (57) leads us to the following regularized global representation of the disturbing potential corresponding to gravity anomalies as boundary data

$$T^\rho(R\xi) = \frac{R}{4\pi}\int_\Omega St^\rho(\xi\cdot\eta)A(R\eta)\,d\omega(\eta) \tag{77}$$

with (see Figure 12)

$$St^\rho(\xi\cdot\eta) \;=\; S^\rho(\xi\cdot\eta) - 6(S(\xi\cdot\eta))^{-1} + 1 - 5\xi\cdot\eta - 3\xi\cdot\eta\,\ln\left(\frac{1}{S^\rho(\xi\cdot\eta)} + \frac{1}{(S^\rho(\xi\cdot\eta))^2}\right). \tag{78}$$

The integrands of $T(R\xi)$ and $T^\rho(R\xi)$ differ only on the spherical cap $\mathcal{S}^\rho(\xi) = \{\eta\in\Omega\big|1-\xi\cdot\eta\le\frac{\rho^2}{2R^2}\}$. Here we have

$$\begin{aligned} St(\xi\cdot\eta) - St^\rho(\xi\cdot\eta) \;=\; & (S(\xi\cdot\eta) - S^\rho(\xi\cdot\eta)) - 3\xi\cdot\eta\,\ln\left(\frac{1}{S(\xi\cdot\eta)} + \frac{1}{(S(\xi\cdot\eta))^2}\right) \\ & +3\xi\cdot\eta\,\ln\left(\frac{1}{S^\rho(\xi\cdot\eta)} + \frac{1}{(S^\rho(\xi\cdot\eta))^2}\right). \end{aligned}$$

Now it follows that for all $t\in[-1,1)$ with $1-t\le\frac{\rho^2}{2R^2}$

$$\begin{aligned} & \ln\left(\frac{1}{S(t)} + \frac{1}{(S(t))^2}\right) - \ln\left(\frac{1}{S^\rho(t)} + \frac{1}{(S^\rho(t))^2}\right) \\ & \quad = \;\ln(1+S(t)) - \ln(1+S^\rho(t)) - 2\left(\ln(S(t)) - \ln(S^\rho(t))\right). \end{aligned} \tag{79}$$

Furthermore, by use of the already known properties of the functions S and S^ρ on $[-1,1)$ we get

$$\left|\ln\left(\frac{1}{S(t)} + \frac{1}{(S(t))^2}\right) - \ln\left(\frac{1}{S^\rho(t)} + \frac{1}{(S^\rho(t))^2}\right)\right| = O(|S(t) - S^\rho(t)|). \tag{80}$$

In connection with (62) we therefore find

$$\lim_{\rho\to 0}\sup_{\xi\in\mathcal{T}}|T(R\xi) - T^\rho(R\xi)| = 0 \tag{81}$$

for every subset $\mathcal{T}\subset\Omega$.

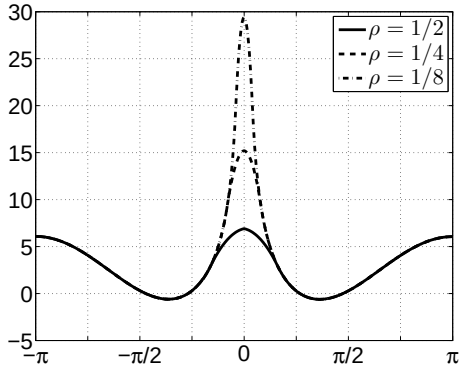

Fig. 14: The regularized Stokes kernel $\vartheta \mapsto St^{\rho}(\cos\vartheta)$ for several ρ.

Next we consider the *Stokes scaling function* $\{St^{\rho_j}\}_{j\in\mathbb{N}_0}$. Correspondingly, the *Stokes wavelets* $\{(WSt)^{\rho_j}\}_{j\in\mathbb{N}_0}$ are given by

$$(WSt)^{\rho_j}(\xi\cdot\eta) = (St)^{\rho_{j+1}}(\xi\cdot\eta) - (St)^{\rho_j}(\xi\cdot\eta), \quad \xi,\eta\in\Omega. \tag{82}$$

In other words, $(\xi,\eta)\mapsto (WSt)^{\rho_j}(\xi\cdot\eta)$, $\xi,\eta\in\Omega$, is a zonal function with local support $\mathcal{S}^{\rho_j}(\xi)$. Its explicit representation reads as follows

$$(WSt)^{\rho_j}(\xi\cdot\eta) \quad = \quad \begin{cases} S^{\rho_{j+1}}(\xi\cdot\eta) - 3\xi\cdot\eta\ln\left(\frac{1}{S^{\rho_{j+1}}(\xi\cdot\eta)} + \frac{1}{(S^{\rho_{j+1}}(\xi\cdot\eta))^2}\right) & \\ -S^{\rho_j}(\xi\cdot\eta) + 3\xi\cdot\eta\ln\left(\frac{1}{S^{\rho_j}(\xi\cdot\eta)} + \frac{1}{(S^{\rho_j}(\xi\cdot\eta))^2}\right), & 0\le 1-\xi\cdot\eta\le\frac{\rho_{j+1}^2}{2R^2} \\ S(\xi\cdot\eta) - 3\xi\cdot\eta\ln\left(\frac{1}{S(\xi\cdot\eta)} + \frac{1}{(S(\xi\cdot\eta))^2}\right) & \\ -S^{\rho_j}(\xi\cdot\eta) + 3\xi\cdot\eta\ln\left(\frac{1}{S^{\rho_j}(\xi\cdot\eta)} + \frac{1}{(S^{\rho_j}(\xi\cdot\eta))^2}\right), & \frac{\rho_{j+1}^2}{2R^2} < 1-\xi\cdot\eta\le\frac{\rho_j^2}{2R^2} \\ 0, & \frac{\rho_j^2}{2R^2} < 1-\xi\cdot\eta\le 2. \end{cases}$$

It should be pointed out that all integrals involving Stokes wavelet functions have not to be extended over the whole sphere. Instead the integral have to be taken over the scale dependent caps $\mathcal{S}^{\rho_j}(\xi)$. Again, a 'zooming-in' procedure to more and more local areas is easily implementable.

6 Modeling of the Disturbing Potential from Deflections of the Vertical by Green Wavelets

The (unique) solution T of the differential equation for the surface gradient

$$\nabla_\xi^* T(R\xi) = -\frac{GM}{R}\Theta(R\xi), \quad \xi\in\Omega, \tag{83}$$

satisfying

$$\int_\Omega T(R\xi)\,d\omega(\xi) = 0, \tag{84}$$

$$\int_\Omega T(R\xi)(\xi\cdot\varepsilon^k)\,d\omega(\xi) = 0, \quad k=1,2,3, \tag{85}$$

can be formulated in terms of Green's function with respect to the Beltrami operator [8], [10] given by

$$G(\xi\cdot\eta) = 1 + \ln\left(\frac{1}{(S(\xi\cdot\eta))^2}\right), \qquad 1-\xi\cdot\eta\neq 0, \tag{86}$$

as follows

$$T(R\xi) = \frac{GM}{4\pi R}\int_\Omega \nabla_\eta^* G(\xi\cdot\eta)\cdot\Theta(R\eta)\,d\omega(\eta), \quad \xi\in\Omega. \tag{87}$$

An easy calculation yields

$$\begin{aligned}\nabla_\eta^* G(\xi\cdot\eta) &= \nabla_\eta^*(1-2\ln(S(\xi\cdot\eta))) \\ &= -2\frac{S'(\xi\cdot\eta)}{S(\xi\cdot\eta)}(\xi-(\xi\cdot\eta)\eta) \\ &= -\frac{1}{2}(S(\xi\cdot\eta))^2(\xi-(\xi\cdot\eta)\eta).\end{aligned} \tag{88}$$

Thus it follows that

$$T(R\xi)=\frac{R}{4\pi}\int_\Omega g(\xi,\eta)\cdot\Theta(R\eta)\,d\omega(\eta), \tag{89}$$

where

$$g(\xi,\eta)=-\frac{GM}{2R^2}(S(\xi\cdot\eta))^2\left(\xi-(\xi\cdot\eta)\eta\right),\quad \xi,\eta\in\Omega. \tag{90}$$

Replacing S by S^ρ we get as regularization T^ρ of T corresponding to deflections of the vertical as data set

$$T^\rho(R\xi)=\frac{R}{4\pi}\int_\Omega g^\rho(\xi,\eta)\cdot\Theta(R\eta)\,d\omega(\eta), \tag{91}$$

where

$$g^\rho(\xi,\eta)=-\frac{GM}{2R^2}(S^\rho(\xi\cdot\eta))^2(\xi-(\xi\cdot\eta)\eta),\quad \xi,\eta\in\Omega. \tag{92}$$

From the properties known for S and S^ρ we are able to derive that

$$\begin{aligned}&\int_\Omega\left((S(\xi\cdot\eta))^2-(S^\rho(\xi\cdot\eta))^2\right)(\xi-(\xi\cdot\eta)\eta)\cdot\Theta(R\eta)\,d\omega(\eta) \\ &= \int_{1-\frac{\rho^2}{2R^2}\le\xi\cdot\eta\le1}\left((S(\xi\cdot\eta))^2-(S^\rho(\xi\cdot\eta))^2\right)\cdot\sqrt{1-(\xi\cdot\eta)^2}\cdot\frac{\xi-(\xi\cdot\eta)\eta}{|\xi-(\xi\cdot\eta)\eta|}\cdot\Theta(R\eta)\,d\omega(\eta) \\ &= O(\rho)\end{aligned} \tag{93}$$

provided that $\Theta(R\cdot)$ is a continuous vector field on Ω. Consequently, we have

$$\lim_{\rho\to0}\sup_{\xi\in\mathcal{T}}|T(R\xi)-T^\rho(R\xi)|=0 \tag{94}$$

for all subsets $\mathcal{T}\subset\Omega$.

Corresponding to the *Green (vector) scaling functions* $\{g^{\rho_j}\}_{j\in\mathbb{N}_0}$ we are able to introduce the *Green wavelets* $\{(Wg)^{\rho_j}\}_{j\in\mathbb{N}_0}$ as follows

$$(Wg)^{\rho_j}(\xi,\eta)=g^{\rho_{j+1}}(\xi,\eta)-g^{\rho_j}(\xi,\eta),\ \xi,\eta\in\Omega. \tag{95}$$

In explicit representation we have

$$(Wg)^{\rho_j}(\xi,\eta) = \begin{cases} -\frac{GM}{2R^2}(S^{\rho_{j+1}}(\xi\cdot\eta))^2(\xi-(\xi\cdot\eta)\eta) & \\ +\frac{GM}{2R^2}(S^{\rho_j}(\xi\cdot\eta))^2(\xi-(\xi\cdot\eta)\eta), & 0\le1-\xi\cdot\eta\le\frac{\rho_{j+1}^2}{2R^2} \\ -\frac{GM}{2R^2}(S(\xi\cdot\eta))^2(\xi-(\xi\cdot\eta)\eta) & \\ +\frac{GM}{2R^2}(S^{\rho_j}(\xi\cdot\eta))^2(\xi-(\xi\cdot\eta)\eta), & \frac{\rho_{j+1}^2}{2R^2}<1-\xi\cdot\eta\le\frac{\rho_j^2}{2R^2} \\ 0, & \frac{\rho_j^2}{2R^2}<1-\xi\cdot\eta\le2. \end{cases}$$

A reconstruction of the disturbing potential T with Green scaling functions and wavelets is shown in Figure 15.

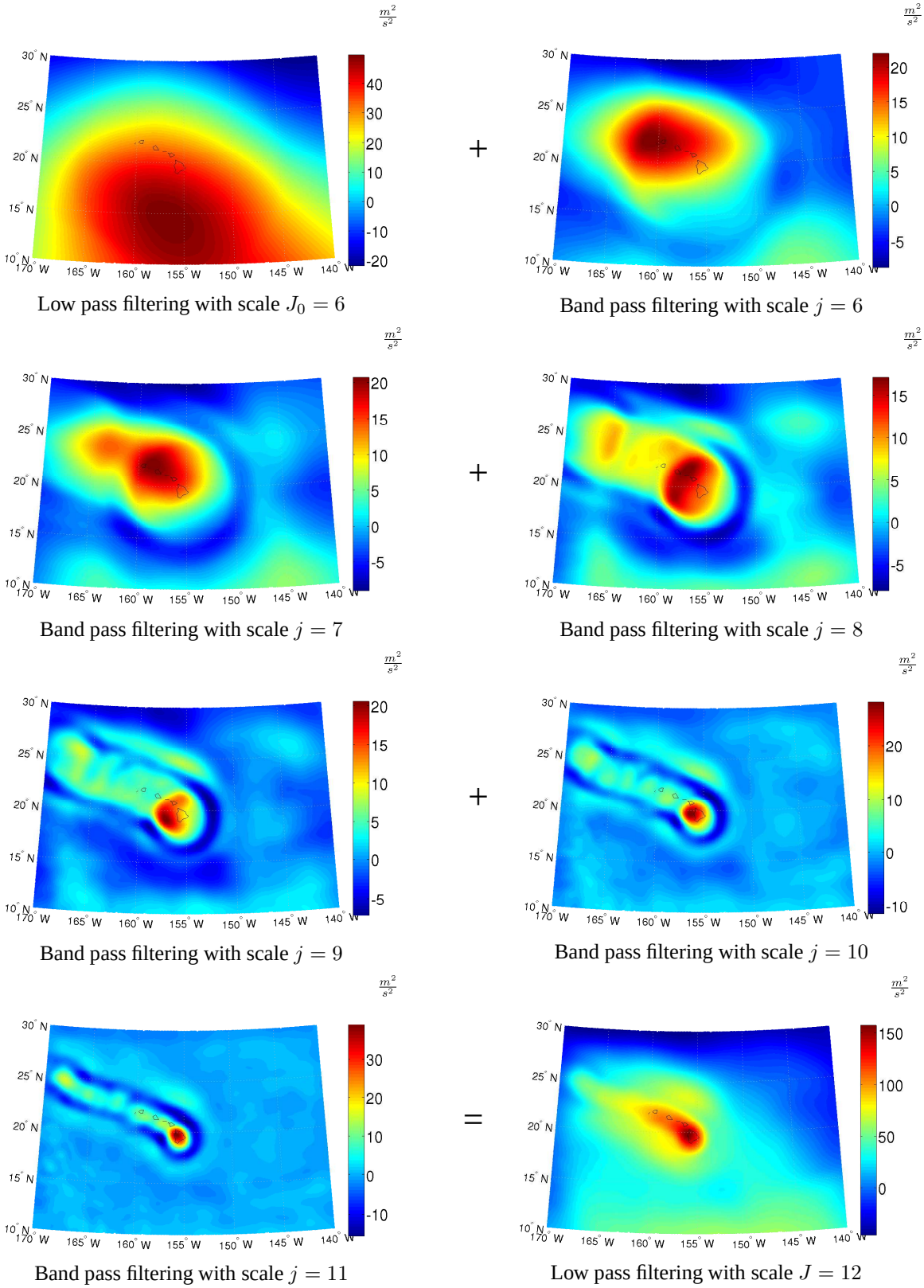

Low pass filtering with scale $J_0 = 6$

Band pass filtering with scale $j = 6$

Band pass filtering with scale $j = 7$

Band pass filtering with scale $j = 8$

Band pass filtering with scale $j = 9$

Band pass filtering with scale $j = 10$

Band pass filtering with scale $j = 11$

Low pass filtering with scale $J = 12$

Fig. 15: Reconstruction of the potential T in $\mathrm{m}^2\mathrm{s}^{-2}$ from vertical deflections in the Hawaiian region using Green wavelets. A rough low pass filtering at scale 6 is improved with several band pass filters of scale 6,...,11. The last illustration shows the approximation of T at scale $J = 12$.

7 Multiscale Approximation

Let $\{\Phi^{\rho_j}\}_{j\in\mathbb{N}_0}$ be one of the scaling functions introduced in this paper (i.e., the Green, Haar, Neumann, or Stokes scaling function). Let us, as usual, denote by $\{(W\Phi)^{\rho_j}\}_{j\in\mathbb{N}_0}$ the associated wavelet function, i.e.,

$$(W\Phi)^{\rho_j} = \Phi^{\rho_{j+1}} - \Phi^{\rho_j}, \quad j \in \mathbb{N}_0. \tag{96}$$

Let $X(R\cdot) : \Omega \to \mathbb{R}$ denote one of the associated (geodetic) quantities occuring in the integral representations (i.e., in the aforementioned order, deflection of the vertical, (observed) signal, gravity disturbance, gravity anomaly).

Summarizing our results we are led to the following 'zooming-in' scheme of multiscale approximation.

Step 1: First we guarantee a 'rough' global (initial) approximation by low pass filtering against the kernel $\Phi^{\rho_{J_0}}$ in form of a convolution integral

$$X^{\rho_{J_0}}(R\xi) = \frac{R}{4\pi}\int_\Omega \Phi^{\rho_{J_0}}(\xi\cdot\eta)X(R\eta)\,d\omega(\eta). \tag{97}$$

Step 2: A first improvement of this rough approximation $X^{\rho_{J_0}}(R\xi)$ by detail information at scale J_0 is provided by adding the band pass filtered version $(WX)^{\rho_{J_0}}$ given by

$$(WX)^{\rho_{J_0}}(R\xi) = \frac{R}{4\pi}\int_\Omega (W\Phi)^{\rho_{J_0}}(\xi\cdot\eta)X(R\eta)\,d\omega(\eta). \tag{98}$$

This yields the approximation of scale J_0+1

$$X^{\rho_{J_0+1}}(R\xi) = X^{\rho_{J_0}}(R\xi) + (WX)^{\rho_{J_0}}(R\xi). \tag{99}$$

As already pointed out, $(WX)^{\rho_{J_0}}(R\xi)$ is the difference between two smoothings. This expression contains the detail information of $X^{\rho_{J_0+1}}(R\xi)$, that is not contained in $X^{\rho_{J_0}}(R\xi)$.

In adaptation to the data situation a (local) 'zooming-in' process gives us the functions $(WX)^{\rho_{J_0}}(R\xi),\dots,(WX)^{\rho_{J_0+k}}(R\xi)$. This yields the (local) approximation of scale J_o+k+1

$$X^{\rho_{J_0+k+1}}(R\xi) = X^{\rho_{J_0}}(R\xi) + \sum_{l=0}^{k}(WX)^{\rho_{J_0+l}}(R\xi). \tag{100}$$

Of course, the numerical evaluation requires the application of approximate integration formulas for $j = J_0,\dots,J_0+k$

$$X^{\rho_j}(R\xi) \simeq \frac{R}{4\pi}\sum_{k=1}^{N_j} w_k^{N_j}\Phi^{\rho_j}(\xi\cdot\eta_k^{N_j})X(R\eta_k^{N_j}), \tag{101}$$

and

$$(WX)^{\rho_j}(R\xi) \simeq \frac{R}{4\pi}\sum_{k=1}^{N_j} w_k^{N_j}(W\Phi)^{\rho_j}(\xi\cdot\eta_k^{N_j})X(R\eta_k^{N_j}), \tag{102}$$

where the summation (102) has to be extended over the scale dependent cap $\mathcal{S}^{\rho_j}$ (the symbol $\simeq$ means that error between the right and left side can be neglected). Obviously, for the every subset $\mathcal{T}\subset\Omega$ the reconstruction formula

$$\sup_{\xi\in\mathcal{T}}\left|X(R\xi) - X^{\rho_{J_0}}(R\xi) - \sum_{l=0}^{\infty}(WX)^{\rho_{J_0+l}}(R\xi)\right| = 0 \tag{103}$$

holds true. The reconstruction ('zooming-in' procedure) is illustrated by the following scheme.

$$\begin{array}{ccccccccccc}
(WX)^{\rho_{J_0}} & & & & (WX)^{\rho_{J_0+1}} & & & & & & \\
& \searrow & & & & \searrow & & & & & \\
X^{\rho_{J_0}} & \longrightarrow & \oplus & \longrightarrow & X^{\rho_{J_0+1}} & \longrightarrow & \oplus & \longrightarrow & X^{\rho_{J_0+2}} & \dots &
\end{array}$$

In consequence, an efficient and economical method based on regularization in space domain has been found for determining globally reflected geodetic quantities of classical physical geodesy from locally available data sets.

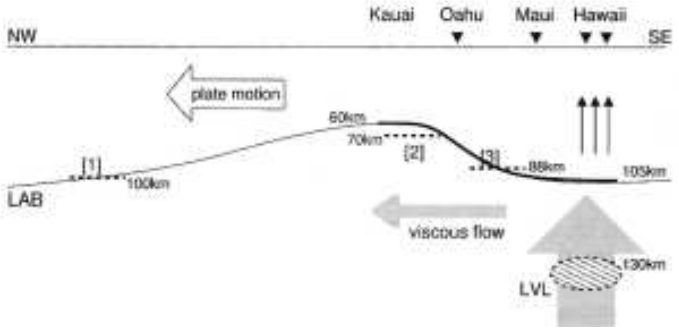

Fig. 16: Conjectured plume configuration for the Hawaiian area (from [45]).

8 Numerical Application: Plume Anomalies

Finally the multiscale techniques presented here will be used to investigate gravity anomalies caused by plumes. Due to their local nature we have to use high resolution gravity data, and the 'zooming-in' approximation as presented here is of great significance. Especially the locally compact (isotropic) smoothed Haar wavelet turns out to be an essential tool of scalar and vectorial multiscale decomposition of gravity disturbances, gravity anomalies, and deflections of the vertical, respectively. As case studies, two prototypes of plumes are chosen, namely the oceanic mid-plate Hawaiian plume and the ridge-centered Iceland plume. They will be discussed in more detail.

Hawaiian Plume - Topographic Description

In global plate tectonics, hotspots and seamount chains are understood as fundamental components nowadays. A stationary mantle plume located beneath the Hawaiian islands is believed to be responsible for the creation of the Hawaii-Emperor seamount chain, while the oceanic lithosphere continuously passed over it. The Hawaii-Emperor chain (see Figure 16) consists of about 100 volcanic islands, atolls, and seamounts that spread nearly 6000 km from the active volcanic island of Hawaii to the 75-80 Ma (million years) old Emperor seamounts nearby the Aleutian trench. With moving further south-east along the island chain, the geological age decreases. The interesting area is the relatively young south-eastern part of the chain, situated on the Hawaiian swell, a 1200 km broad anomalously shallow region of the ocean floor, extending from the island of Hawaii to the Midway atoll. Here a distinct geoid anomaly occurs that has its maximum around the youngest island that coincides with the maximum topography and both decrease in north-west direction.

The progressive decrease in terms of the geological age is believed to result from the continuous motion of the underlaying plate or, to be more specific, from the motion of the pacific lithosphere over a stationary mantle plume beneath the youngest island (cf. [29], [30], [43]).

This plume is supposed to have its origin in the lower mantle (see [21], [29]) or even rise from the core mantle boundary (cf. [38]). The excess temperature of the plume is assumed to be more than $200°C$ and the hot mantle material is expected to run from the origin up to the upper mantle in a narrow stem with a radius of about 100-200 km (see [31]). With seismic tomography several features of the Hawaiian mantle plume are detected (cf. [35]). The results deliver a so-called low velocity zone (LVZ) beneath the lithosphere, starting at a depth of about 130-140 km, beneath the central part of the island of Hawaii. This LVZ is interpreted as an indication for a partial melting zone localized inside the plume conduit. So-called P receiver functions suggested an 40 km large uplift in the mantle transition zone at a depth of 660 km, caused by the rising mantle plume. An in north-west direction increasing shallow of the oceanic lithosphere was obtained with S receiver functions, that have been interpreted to suggest a thermal rejuvenation of the lithosphere caused by the Hawaiian mantle plume. The interested reader may be referred to [35] and the references therein.

Dataset and Implementation

The gravity data used for our numerical computation represent the gravity anomalies around the islands of Hawaii. Because of the lack of terrestrial-only data, we used the combined gravity model EIGEN-GL04C consisting of satellite data, gravimetry, and altimetry surface data. The dataset used to calculate the gravity anomalies was provided by the GFZ-Potsdam. The sequence $\rho_j = 2^{-j}$ is chosen for gravity anomaly modeling and a smoothed Haar kernel of a polynomial degree of $k = 5$ turned out to be advantageous for our purposes. Since the kernel function has local support we can restrict our considerations to the local area of interest. So the illustrations are calculated on a 350×350 pointgrid around the island of Hawaii, taken from a 5000×5000 longitute-latitude grid (of type [3]). The scalar and vectorial solutions are shown in Figure 17 and Figure 18.

In the multiscale analysis several interesting observations can be detected. By comparing the different positions ξ and different scales j, we can see that the local maximum of the energy, that corresponds to the the wavelet variances (see [11], [27]), contained in the signal of the gravity anomalies starts in the north-west of the Hawaiian islands for scale 2 and travels

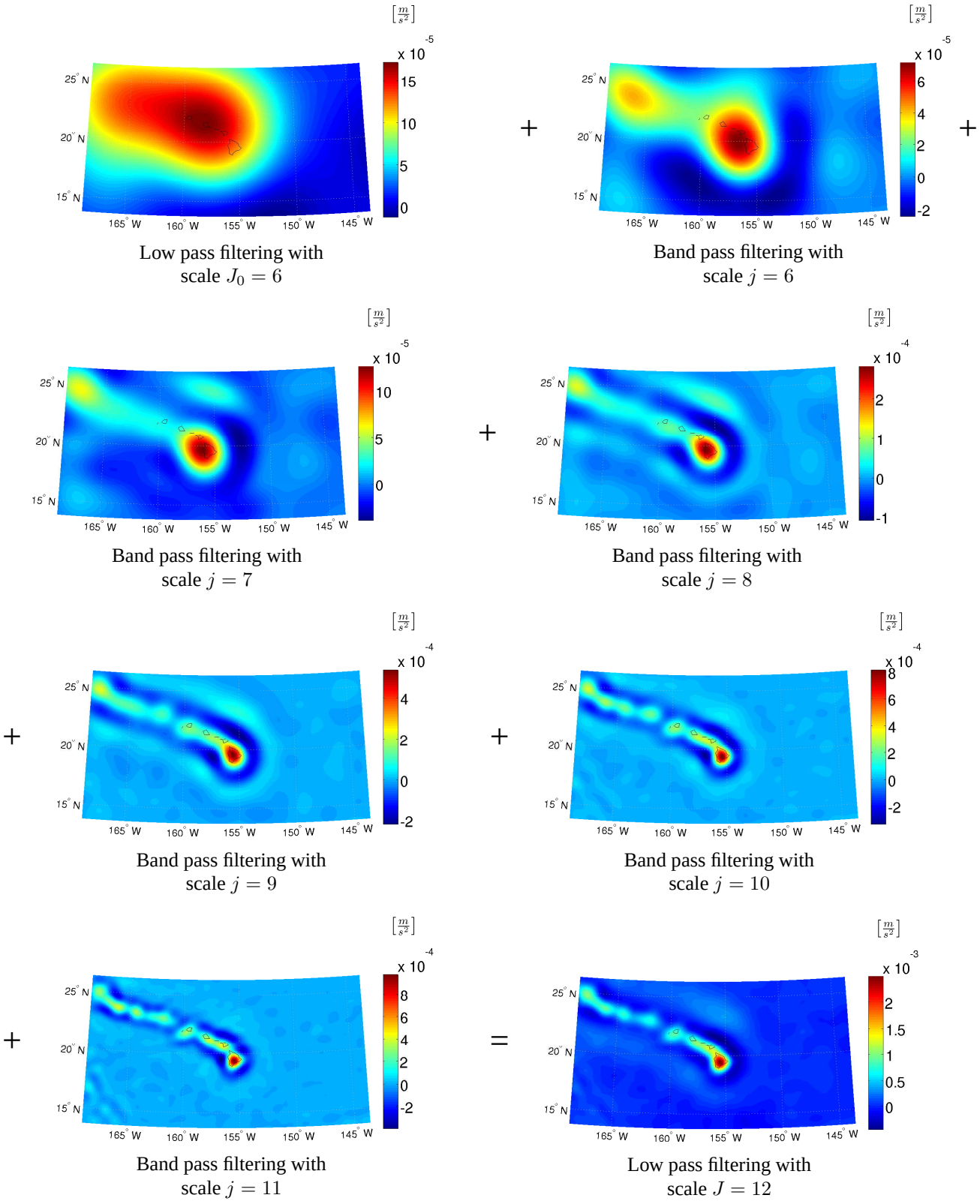

Low pass filtering with scale $J_0 = 6$

Band pass filtering with scale $j = 6$

Band pass filtering with scale $j = 7$

Band pass filtering with scale $j = 8$

Band pass filtering with scale $j = 9$

Band pass filtering with scale $j = 10$

Band pass filtering with scale $j = 11$

Low pass filtering with scale $J = 12$

Fig. 17: Approximation of the gravity anomalies A in ms^{-2} of the Hawaiian region with smoothed Haar wavelets. A rough low pass filtering at scale 6 is improved with several band pass filters of scale 6,...,11.

in south-east direction with increasing scale. It ends up, for scale $J = 12$, in a position at the geologically youngest island under which the mantle plume is assumed to exist. Again, in the multiresolution property with increasing scale, more and

more local details of the gravity anomalies appear. The structure of the Hawaiian island chain is clearly reflected in the scale and space decomposition, as discovered in the global multiscale analysis. Obviously, the energy peak observed at the youngest island of Hawaii is highly above the energy intensity of the rest of the island chain. This seems to strongly corroborate the belief of a mantle plume just below the main island of Hawaii. Similar results are also developable from deflections of the vertical by using Green wavelets (see Figure 15).

Iceland Plume - Topographic Description

The plume beneath Iceland is the prototype of a ridge-centered mantle plume. An interaction between the North Atlantic ridge and the mantle plume is believed to be the reason for the existence of Iceland, resulting in melt production and crust generation since the continental break-up in the late Palaeocene and early Eocene 58 Ma ago. Nevertheless, there is still no agreement on the location of the plume before rifting started in the east. Controversal discussions, whether it was located under central or eastern Greenland about 62-64 Ma ago are still in progress (cf. [35]).

Iceland itself represents the top of a nearly circular rise topography, with the maximum of about 2.8 km above the surrounding seafloor in the South of the glacier 'Vatnajökull'. This glacier is the largest European one and several active volcanoes are located beneath it, which are supposed to be feeded by a mantle plume. The surrounding oceanic crust consists of three different types involving a crust thickness that is more than three times as thick as average oceanic crusts. Seismic tomography provides evidence of the existence of a mantle plume beneath Iceland, resulting in low velocity zones in the upper mantle and the transition zone, but also hints for anomalies in the deeper mantle seem to exist. The low velocity anomalies have been detected in depths ranging from at least 400 km up to about 150 km in regional P-wave models. Above 150 km ambiguous seismic velocity structures were obtained involving regions of low velocities covered by regions of high-seismic-velocities. Furthermore low S-wave velocities at a depth of about 80 km were indicated by special surface wave dispersion data, as well (cf. [25]). For a deeper access into the theory of the Iceland plume the interested reader may be referred to [25], [26], [35] and the references therein.

Dataset and Implementation

The gravity data decomposed here represent the gravity anomalies around Iceland. The dataset used to calculate the gravity anomalies has the same high resolution gravity model as used in the Hawaiian case study. Again the sequence $\rho_j = 2^{-j}$ is chosen and the smoothed Haar kernel has a polynomial degree of $k = 5$. Since the kernel function has local support we can restrict our considerations to the local area of interest. To avoid a boundary influence by the surrounding topography, which was negligible in the Hawaiian case study, we calculate our multiscale decomposition on a larger point grid (300×300) around the Iceland hotspot. So the illustration are restricted to a grid of 200×200 gridpoints around Iceland, taken from a 5000×5000 longitude-latitude grid of type [3]. The scalar solutions are shown in Figure 19.

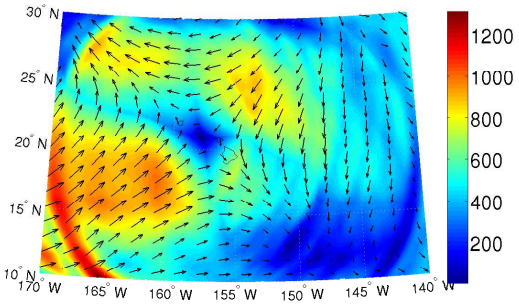

Low pass filtering with scale $J_0 = 6$

+

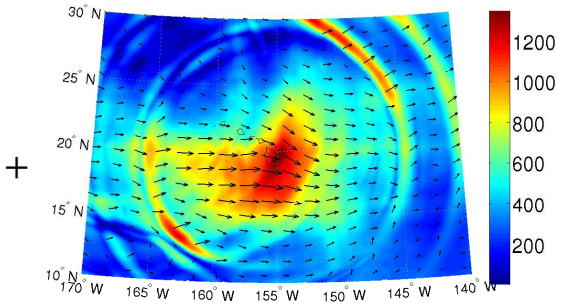

Band pass filtering with scale $j = 6$

+

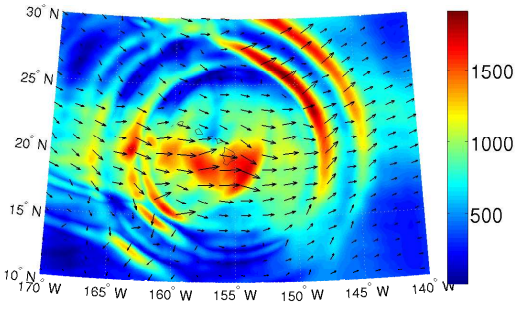

Band pass filtering with scale $j = 7$

+

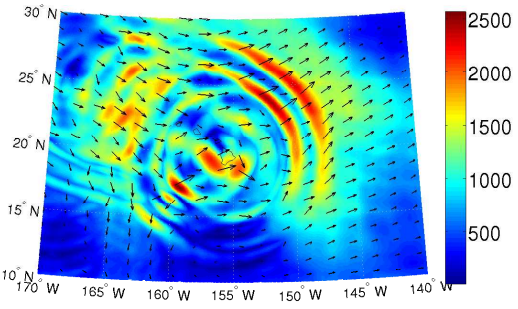

Band pass filtering with scale $j = 8$

+

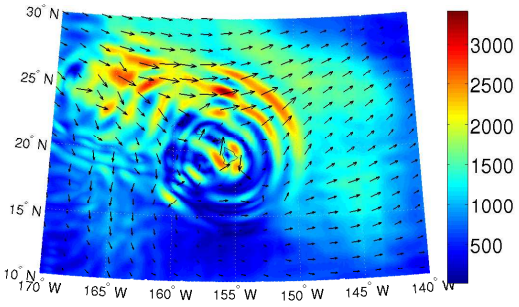

Band pass filtering with scale $j = 9$

+

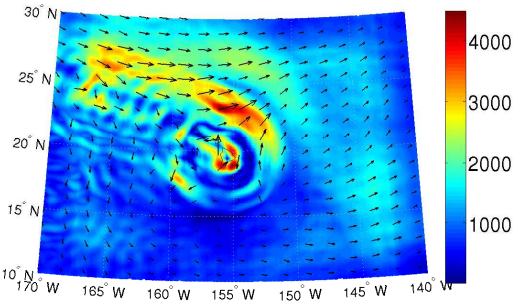

Band pass filtering with scale $j = 10$

+

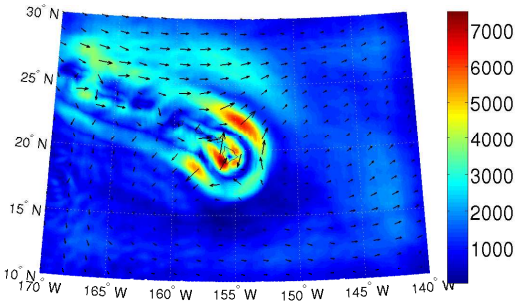

Band pass filtering with scale $j = 11$

=

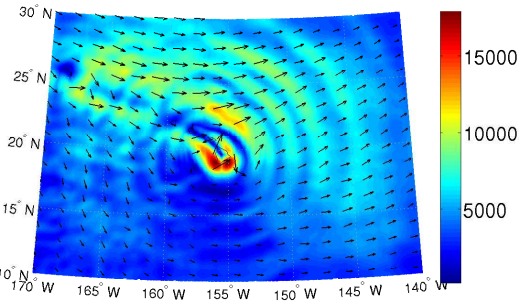

Low pass filtering with scale $J_0 = 12$

Fig. 18: Approximation of the vector valued vertical deflections Θ of the Hawaiian region with smoothed Haar wavelets. A rough low pass filtering at scale 6 is improved with several band pass filters of scale 6,...,11. The last picture shows the multiscale approximation at scale $J = 12$.

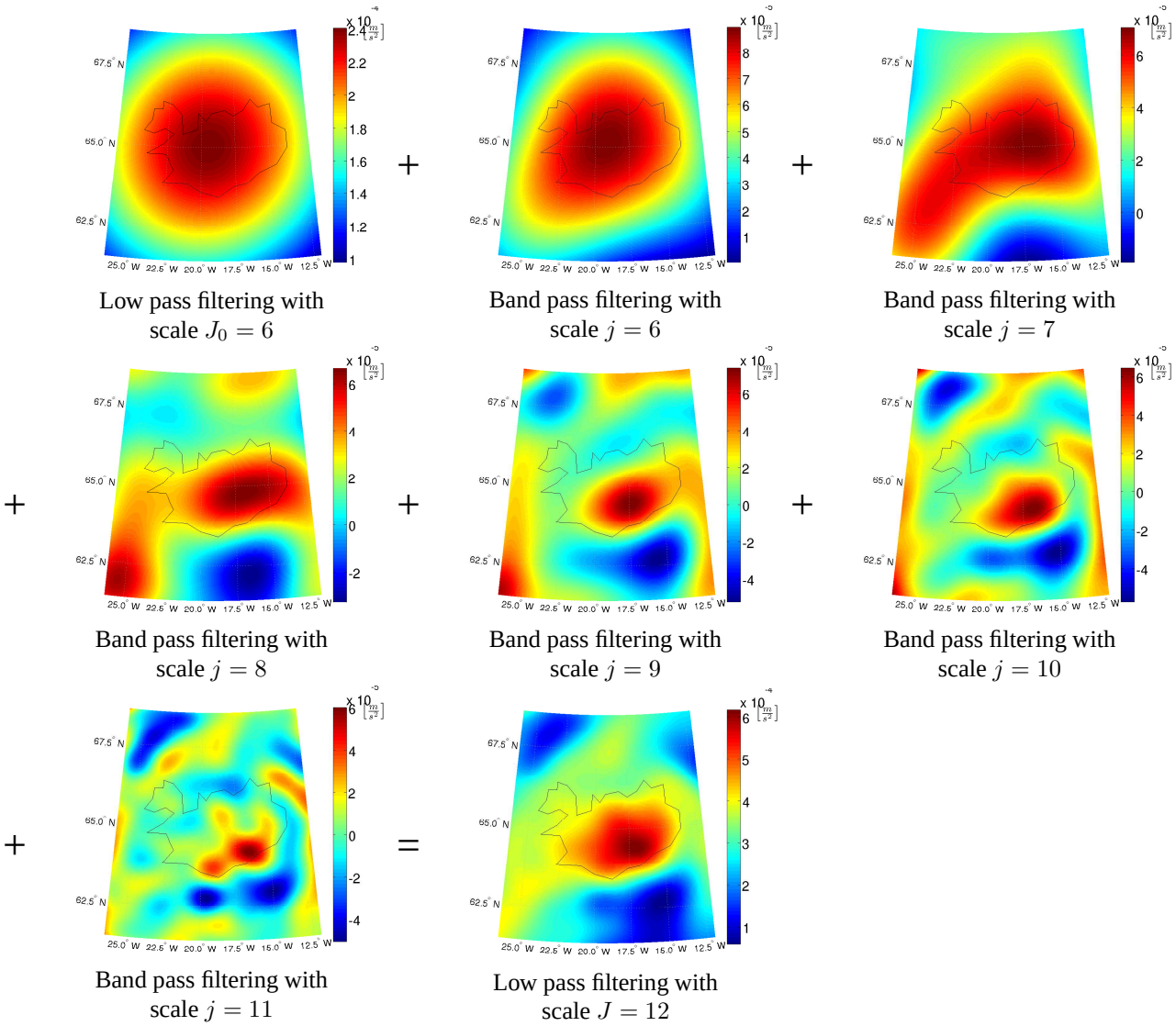

Fig. 19: Approximation of the gravity anomalies A in ms^{-2} of Iceland with smoothed Haar wavelets. A rough low pass filtering at scale 6 is improved with several band pass filters of scale 6,...,11. The last illustration shows the multiscale approximation at scale $J = 12$.

Some quite interesting observations can be made by looking at the multiscale analysis. In the lower scales (not shown here) the shape and the center of the signal energy dos not vary remarkably. However, from scale 6 on, the energy analyzed in the signal travels towards the south-west along the North Atlantic ridge and the center of the 'peak' situated on Iceland moves south-eastwards along the Greenland-Iceland-Faeroer ridge. In the high scales 9, 10, and 11 the anomaly in the south-east dominates significantly. This anomaly located in the south-east of Iceland may be interpreted as the signal of the mantle plume beneath Iceland. Since this anomaly clearly manifests in the high scales, its spatial extension has to be rather small, which coincides with seismic observations, limiting the radial diameter of the upper part of mantle plumes to about 100 - 150 km.

9 Conclusions

The purpose of this paper is to demonstrate that locally (space) supported wavelets provide a powerful approximation technique for the investigation of, e.g., local fine-structured features such as those caused by plumes. The illustrations show that the presented multiscale procedure allows a scale and space dependent characterization of this geophysical phenomenon. As approximate integration rules fast longitude-latitude grids (as proposed by [3], [44]) have been used; especially in the case study of the Hawaii plume, which has also been discussed in several papers involving seismic tomography (see, e.g.,

[45]), we can achieve comparable results for the spatial position of the anomaly caused by the plume. In fact, the wavelet coefficients can be interpreted as spatial measures of certain frequency bands contained in the signal. Thereby, the wavelet theory offers an applicable physical approach for detecting plume features.

Concerning the Hawaii plume in more detail, the numerical results show us that the anomaly is located on a north-west to south-east line below the Hawaiian islands. As the wavelength part of a signal is associated to depth we can also conclude that the deep parts of the plume, which correspond to the lower scales, are centered below the islands Maui and Oahu. The higher scales, corresponding to the upper part of the plume, can be localized directly below Hawaii.

Acknowledgements This work is supported by the 'Deutsche Forschungsgemeinschaft' (DFG) and the 'Bundesministerium für Bildung und Forschung' (BMBF). M. Klug and D. Mathar participate in the DFG SPP priority programme 1257, especially in the Project Mantle Plumes and the Geoid. Kerstin Wolf is supported by the programme "Geotechnologien - Erfassung des Systems Erde aus dem Weltraum" (Projektleitung: Prof. Dr. Markus Rothacher (GFZ, Potsdam), Prof. Dr. R. Dietrich (TU Dresden), Prof. Dr. P. Döll (UFM Frankfurt), Prof. Dr. W. Freeden (TU Kaiserslautern), Förderkennzeichen: 03F0424-D). We also have to thank the GFZ Potsdam for providing us with gravity data for the Hawaiian and Iceland areas.

References

[1] A.A. Aardalan, E.W. Grafarend, G. Finn, Ellipsoidal Vertical Deflections and Ellipsoidal Gravity Disturbances: Case Studies, Stud. Geophys. Geod., 50, 1–57 (2006).
[2] E.H. Bruns, Die Figur der Erde, Publikation Königl. Preussisch. Geodätisches Institut, P. Stankiewicz Buchdruckerei, Berlin (1878).
[3] J.R. Driscoll and R.M. Healy, Computing Fourier Transforms and Convolutions on the 2-Sphere, Advances in Applied Mathematics, 15, 202-250 (1994).
[4] ESA, The Nine Candidate Earth Explorer Missions, Publications Division ESTEC, Noordwijk, SP-1196(1) (1996).
[5] ESA, European Views on Dedicated Gravity Field Missions: GRACE and GOCE, ESD–MAG–REP–CON–001 (1998).
[6] ESA, Gravity Field and Steady-State Ocean Circulation Mission, ESTEC, Noordwijk, ESA SP–1233(1) (1999).
[7] M.J. Fengler, W. Freeden, M.Gutting, Darstellung des Gravitationsfeldes und seiner Funktionale mit sphärischer Multiskalentechnik. ZfV, 323-334 (2004).
[8] W. Freeden, Über eine Klasse von Integralformeln der Mathematischen Geodäsie, Veröff. Geod. Inst. RWTH Aachen (1979).
[9] W. Freeden, Multiscale Modelling of Spaceborne Geodata, Teubner, Stuttgart, Leipzig (1999).
[10] W. Freeden, T. Gervens, and M. Schreiner, Constructive Approximation on the Sphere (With Application to Geomathematics), Oxford Sciences Publication, Clarendon Press, (1998).
[11] W. Freeden, T. Maier, In Multiscale Denoising of Spherical Functions: Basic Theory and Numerical Aspects, Electronic Transactions on Numerical Analysis (ETNA), 14:40-62 (2002).
[12] W. Freeden, K. Wolf, Klassische Erdschwerefeldbestimmung aus der Sicht moderner Geomathematik, Schriften der Funktionalanalysis und Geomathematik, Bericht Nr. 38, Technische Universität Kaiserlautern (2008).
[13] C.F. Gauss, Bestimmung des Breitenunterschiedes zwischen den Sternwarten von Göttingen und Altona, Vandenhoek und Ruprecht, Göttingen (1828).
[14] E. Groten, Geodesy and the Earth's Gravity Field I,II, Dümmler (1979).
[15] A. Haar, Zur Theorie der orthogonalen Funktionsysteme. Math. Ann. 69: 331-371 (1910).
[16] W.A. Heiskanen, H. Moritz, Physical Geodesy, W.H. Freeman and Company, San Francisco (1967).
[17] B. Hoffmann-Wellendorf, H. Moritz, Physical Geodesy, Springer, Wien, New York (2005).
[18] F.R. Helmert, Die mathematischen und physikalischen Theorien der Höheren Geodäsie, 1, B.G. Teubner Verlagsgesellschaft Leipzig (1880).
[19] F.R. Helmert, Die mathematischen und physikalischen Theorien der Höheren Geodäsie, 2, B.G. Teubner Verlagsgesellschaft Leipzig (1884).
[20] F. Jakobs, H. Meyer, Geophysik – Signale aus der Erde, Teubner, Leipzig (1992).
[21] Y. Ji and H.-C. Nataf, Detection of Mantle Plumes in the Lower Mantle by Diffraction Tomography: Hawaii, Earth Planet Sci Lett, 159: 99-115, (1998).
[22] F.G. Lemoine, S.C. Kenyon, J.K. Factor, R.G. Trimmer, N.K. Pavlis, D.S. Chinn, C.M. Cox, S.M. Klosko, S.B. Luthcke, M.H. Torrence, Y.M. Wang, R.G. Williamson, E.C. Pavlis, R.H. Rapp, T.R. Olson, The Development of the Joint NASA GSFC and NIMA Geopotential Model EGM96, NASA/TP-1998-206861 (1998).
[23] O.D. Kellogg, Foundation of Potential Theory, Springer, Berlin, Heidelberg, New York (1967).
[24] J.B. Listing, Über unsere jetzige Kenntnis der Gestalt und Größe der Erde, Dietrichsche Verlagsbuchhandlung, Göttingen (1873).
[25] G. Marquart and H. Schmeling, A Dynamic Model for the Iceland Plume and the Atlantic Based on Tomography and Gravity Data, Geophys. J. Int., 159: 40-52, (2004).
[26] H. Schmeling and G. Marquart, Crustal Accretion and Dynamic Feedback on Mantle Melting of a Ridge Centred Plume: The Iceland Case, Tectonophysics, Special Volume "Plate motion and crustal processes in and around Iceland", (2005).
[27] D. Mathar, Wavelet Variances and Their Application in Geoscientifically Relevant Feature Detection, Diploma Thesis, University of Kaiserslautern, Geomathematics Group (2008).

[28] P. Meissl, On the Linearization of the Geodetic Boundary Value Problem, Reports of the Department of Geodetic Science, No. 152, The Ohio State University, Columbus (1971).
[29] W.J. Morgan, Convective Plumes in the Lower Mantle, Nature, 230: 42-43, (1971).
[30] W.J. Morgan, J.P. Morgan and E. Price, Hotspot Melting Generates Both Hotspot Volcanism and a Hotspot Swell, J Geophysical Res, 100: 8054-8062, (1995).
[31] H.-C. Nataf, Seismic Imaging of Mantle Plumes, Ann Rev Earth Planet Sci, 28: 391-417, (2000).
[32] F. Neumann, Vorlesungen über die Theorie des Potentials und der Kugelfunktionen, Teubner, Leipzig, 135-154 (1887).
[33] P. Pizzetti, Sopra il calcoba tesrico delle deviazioni del geoide dall' ellissoide, Att R Accad Sci Torino, 46: 331-350 (1910).
[34] P. Pizzetti, Geodesia - Sulla espressione della gravita alla superficie del geoide, supposto ellissoidico, Atti Reale Accademia dei Lincei 3, 166-172 (1894).
[35] J.R.R. Ritter and U.R. Christensen, Mantle Plumes, A Multidisciplinary Approach, Springer-Verlag Berlin Heidelberg, (2007).
[36] R. Rummel, Geodesy, Encyclopedia of Earth System Science. Vol. 2, p. 253-262, Akademic Press (1992).
[37] R. Rummel, G. Balmino, J. Johannessen, P. Visser, P. Woodworth, Dedicated Gravity Field Missions - Principles and Aims, J. of Geodynamics, 33: 3-20 (2002).
[38] S.A. Russel, T. Lay, and E.J. Garnero, Seismic Evidence for Small-Scale Dynamics in the Lower Most Mantle at the Root of the Hawaiian Hotspot, Nature, 396: 255-258, (1998).
[39] W. Torge, Geodesy, de Gruyter, Berlin (1991).
[40] G. G. Stokes, On the Variation of Gravity at the Surface of the Earth, Trans. Cambr. Phil. Soc., 8: 672-712. In: Mathematical and Physical Papers by George Gabriel Stokes, Vol. II. Johnson Reprint Corporation, New York, 131-171 (1849).
[41] A. Wangerin, Theorie des Potentials und der Kugelfunktionen, Vereinigung wissenschaftlicher Verlag Walter de Gruyter & Co, Berlin, Leipzig (1921).
[42] H. Weyl, Über die Gleichverteilung von Zahlen mod Eins. Math. Ann. 77:313-352 (1916).
[43] J.T. Wilson, A Possible Origin of the Hawaiian Island, Can J Phys, 41: 863-868 (1963).
[44] K. Wolf, Numerical Aspects of Harmonic Spline-Wavelets for the Satellite Gravimetry Problem, Diploma Thesis, University of Kaiserslautern, Geomathematics Group (2006).
[45] X. Yuan, X. Li, I. Wölbern, and R. Kind, Tracing the Hawaiian Mantle Plume by Converted Seismic Waves, In: Mantle Plumes (J.R.R. Ritter, U.R. Christensen, eds), 49-70, Springer (2007).

Folgende Berichte sind erschienen:

2003

Nr. 1 S. Pereverzev, E. Schock.
On the adaptive selection of the parameter in regularization of ill-posed problems

Nr. 2 W. Freeden, M. Schreiner.
Multiresolution Analysis by Spherical Up Functions

Nr. 3 F. Bauer, W. Freeden, M. Schreiner.
A Tree Algorithm for Isotropic Finite Elements on the Sphere

Nr. 4 W. Freeden, V. Michel (eds.)
Multiscale Modeling of CHAMP-Data

Nr. 5 C. Mayer
Wavelet Modelling of the Spherical Inverse Source Problem with Application to Geomagnetism

2004

Nr. 6 M.J. Fengler, W. Freeden, M. Gutting
Darstellung des Gravitationsfeldes und seiner Funktionale mit Multiskalentechniken

Nr. 7 T. Maier
Wavelet-Mie-Representations for Soleniodal Vector Fields with Applications to Ionospheric Geomagnetic Data

Nr. 8 V. Michel
Regularized Multiresolution Recovery of the Mass Density Distribution From Satellite Data of the Earth's Gravitational Field

Nr. 9 W. Freeden, V. Michel
Wavelet Deformation Analysis for Spherical Bodies

Nr. 10 M. Gutting, D. Michel (eds.)
Contributions of the Geomathematics Group, TU Kaiserlautern, to the 2nd International GOCE User Workshop at ESA-ESRIN Frascati, Italy

Nr. 11 M.J. Fengler, W. Freeden
A Nonlinear Galerkin Scheme Involving Vector and Tensor Spherical Harmonics for Solving the Incompressible Navier-Stokes Equation on the Sphere

Nr. 12 W. Freeden, M. Schreiner
Spaceborne Gravitational Field Determination by Means of Locally Supported Wavelets

Nr. 13 F. Bauer, S. Pereverzev
Regularization without Preliminary Knowledge of Smoothness and Error Behavior

Nr. 14 W. Freeden, C. Mayer
Multiscale Solution for the Molodensky Problem on Regular Telluroidal Surfaces

Nr. 15 W. Freeden, K. Hesse
Spline modelling of geostrophic flow: theoretical and algorithmic aspects

2005

Nr. 16 M.J. Fengler, D. Michel, V. Michel
Harmonic Spline-Wavelets on the 3-dimensional Ball and their Application to the Reconstruction of the Earth's Density Distribution from Gravitational Data at Arbitrarily Shape Satellite Orbits

Nr. 17 F. Bauer
Split Operators for Oblique Boundary Value Problems

Nr. 18 W. Freeden, M. Schreiner
Local Multiscale Modelling of Geoidal Undulations from Deflections of the Vertical

Nr. 19 W. Freeden, D. Michel, V. Michel
Local Multiscale Approximations of Geostrophic Flow: Theoretical Background and Aspects of Scientific Computing

Nr. 20 M.J. Fengler, W. Freeden, M. Gutting
The Spherical Bernstein Wavelet

Nr. 21 M.J. Fengler, W. Freeden,
A. Kohlhaas, V. Michel, T. Peters
Wavelet Modelling of Regional and Temporal Variations of the Earth's Gravitational Potential Observed by GRACE

Nr. 22 W. Freeden, C. Mayer
A Wavelet Approach to Time-Harmonic Maxwell's Equations

Nr. 23 M.J. Fengler, D. Michel, V. Michel
Contributions of the Geomathematics Group to the GAMM 76th Annual Meeting

Nr. 24 F. Bauer
Easy Differentiation and Integration of Homogeneous Harmonic Polynomials

Nr. 25 T. Raskop, M. Grothaus
On the Oblique Boundary Problem with a Stochastic Inhomogeneity

2006

Nr. 26 P. Kammann, V. Michel
Time-Dependent Cauchy-Navier Splines and their Application to Seismic Wave Front Propagation

Nr. 27 W. Freeden, M. Schreiner
Biorthogonal Locally Supported Wavelets on the Sphere Based on Zonal Kernel Functions

Nr. 28 V. Michel, K. Wolf
Numerical Aspects of a Spline-Based Multiresolution Recovery of the Harmonic Mass Density out of Gravity Functionals

Nr. 29 V. Michel
Fast Approximation on the 2-Sphere by Optimally Localizing Approximate Identities

Nr. 30 M. Akram, V. Michel
Locally Supported Approximate Identities on the Unit Ball

2007

Nr. 31 T. Fehlinger, W. Freeden,
S. Gramsch, C. Mayer, D. Michel, and M. Schreiner
Local Modelling of Sea Surface Topography from (Geostrophic) Ocean Flow

Nr. 32 T. Fehlinger, W. Freeden,
C. Mayer, and M. Schreiner
On the Local Multiscale Determination of the Earth's Disturbing Potential From Discrete Deflections of the Vertical

Nr. 33 A. Amirbekyan, V. Michel
Splines on the 3-dimensional Ball and their Application to Seismic Body Wave Tomography

Nr. 34 W. Freeden, D. Michel, V. Michel
Product Framelet Based Operator Decomposition

Nr. 35 M. Schreiner
The Role of Tensor Fields for Satellite Gravity Gradiometry

Nr. 36 H. Nutz, K. Wolf
Time-Space Multiscale Analysis by Use of Tensor Product Wavelets and its Application to Hydrology and GRACE Data

2008

Nr. 37 W. Freeden, M. Gutting
On the Completeness and Closure of Vector and Tensor Spherical Harmonics

Nr. 38 W. Freeden, K. Wolf
Klassische Erdschwerefeld-bestimmung aus der Sicht moderner Geomathematik

Nr. 39 W. Freeden, T. Fehlinger, M. Klug, D. Mathar, K. Wolf
Classical Globally Reflected Gravity Field Determination in Modern Locally Oriented Multiscale Framework

TECHNISCHE UNIVERSITÄT
KAISERSLAUTERN

Informationen:

Prof. Dr. W. Freeden
Prof. Dr. E. Schock
Fachbereich Mathematik
Technische Universität Kaiserslautern
Postfach 3049
D-67653 Kaiserslautern
E-Mail: freeden@mathematik.uni-kl.de
schock@mathematik.uni-kl.de